

Hepatitis B virus surface antigen drives T cell immunity through non-canonical antigen presentation in mice

Received: 25 July 2024

Accepted: 7 May 2025

Published online: 17 May 2025



Xiaofang Li^{1,3}, Wenxuan Sun^{1,3}, Xiaolan Xu¹, Qirong Jiang², Yuheng Shi¹, Huixi Zhang¹, Weien Yu², Bisheng Shi¹, Simin Wan¹, Jiangxia Liu¹, Wuhui Song¹, Jiming Zhang², Zhenghong Yuan¹✉ & Jianhua Li¹✉

Hepatitis B virus (HBV) exclusively infects hepatocytes and produces large amounts of subviral particles containing its surface antigen (HBsAg). T cell immunity is crucial for controlling and clearing HBV infection. However, the intercellular processes underlying HBsAg presentation to T cells are incompletely understood. Here, using preclinical mouse models, we show that, following HBsAg expression, the intrahepatic Batf3⁺XCRI⁺CCR7⁺ conventional dendritic cell subset cDC1 presents HBsAg by MHC-I cross-dressing, driving CD8⁺ T cell response. Meanwhile, upon HBsAg access to lymphoid tissues, B cells acquire HBsAg directly in the follicles of lymphoid tissues and initiate CD4⁺ T cell responses sequentially in the follicular and interfollicular regions, guided by chemoattractant receptors CCR5 and EBI2, respectively. Finally, we identify ALCAM, LFA-1, and CD80 as key co-stimulatory signals essential for optimal T cell responses. Thus, these findings reveal the roadmap of non-canonical antigen presentation that drives T cell immunity against HBsAg, advancing novel therapeutic strategies for chronic HBV infection.

Hepatitis B virus (HBV) infection is a significant global public health threat, with over 240 million individuals chronically infected worldwide, leading to approximately 650,000 deaths annually from cirrhosis and hepatocellular carcinoma¹. HBV, a member of the *Hepadnaviridae* family, comprises a nucleocapsid, containing partially double-stranded, relaxed circular DNA (rcDNA) and HBV core antigen (HBcAg), enveloped by HBV surface antigen (HBsAg) embedded within a lipid membrane². The rcDNA forms a covalently closed circular DNA (cccDNA) within the nucleus of the host cell, which serves as a template for transcription of viral mRNAs³. Infected cells produce 10²–10⁵ times more subviral particles of HBV, which contain HBsAg, than they do infectious virions⁴. Resolution of acute infection by the immune system involves the clearance of HBsAg and the development of anti-HBsAg antibodies^{5–8}; however, cccDNA may continue to persist in liver

cells⁹. Currently, the goal of therapy for chronic HBV infection is sustained loss of HBsAg, with or without anti-HBsAg seroconversion, leading to a functional cure^{10,11}. However, current treatments rarely achieve this¹⁰. Thus, there is an urgent need to better understand the immune response to HBsAg, which will enable the development of novel therapeutics.

T cell immunity is crucial for controlling and clearing HBV infection^{5–8}. While CD8⁺ T cells play a central role in this process, CD4⁺ T cells orchestrate both CD8⁺ T cell and antibody responses, and act as direct effectors of antiviral immunity^{5–8}. T cell immune responses constitute a complex and well-coordinated network involving various cells, mediators, and niches¹². This network's functionality hinges on the presentation of antigens from sites of viral replication, such as the liver in the case of HBV, to T cells, which are predominantly located in

¹Key Laboratory of Medical Molecular Virology (MOE/NHC/CAMS), Shanghai Institute of Infectious Disease and Biosecurity, Shanghai Frontiers Science Center of Pathogenic Microorganisms and Infection, School of Basic Medical Sciences, Shanghai Medical College, Fudan University, Shanghai, China. ²Department of Infectious Diseases, Huashan Hospital, Fudan University, Shanghai, China. ³These authors contributed equally: Xiaofang Li, Wenxuan Sun.

✉ e-mail: zhuyuan@shmu.edu.cn; jianhuali@fudan.edu.cn

secondary lymphoid organs but are also present in peripheral tissues. The crucial task of antigen presentation is executed by specific cells, known as antigen-presenting cells (such as dendritic cells, macrophages, and B cells)^{13–17}. Our current understanding of viral antigen presentation primarily stems from studying viruses with tropism for both peripheral and lymphoid tissues, or from immunization with various adjuvant-antigen combinations^{16–20}. According to these studies, T cells are primed in the T cell zone of the spleen and draining lymph nodes (dLN) by conventional dendritic cells (cDC) after their acquisition of antigens. The cDC1 subset employs MHC class I (MHC-I) cross-presentation to activate CD8⁺ T cell differentiation. In contrast, the cDC2 subset utilizes MHC class II (MHC-II) to present antigens to CD4⁺ T cells, thereby triggering their differentiation, which includes initiating the early stages of T follicular helper (Tfh) cell differentiation¹³. In parallel, B cells in the follicles of lymphoid tissues capture antigens from CD169⁺ resident macrophages and migrate to the interface between the B cell follicle and the T cell zone (T-B border), enhancing Tfh cell maturation²¹. In these research scenarios, the immune system is exposed to a wealth of innate immune ligands and readily accessible antigens^{22,23}, thereby enabling it to mount an effective T cell immune response. However, HBV's exclusive hepatotropism², along with its failure to elicit an apparent innate immune response^{5–8}, presents a significant challenge for the immune system's ability to detect and acquire viral antigens. Thereby, the applicability of the above-described principles of antigen presentation to HBsAg remains uncertain. Despite this distinctive situation, the key intercellular processes by which HBsAg is presented to T cells, thus inducing T cell immune responses, remain largely unexplored.

Mouse models remain essential for investigating complex immune responses to viruses. Despite the inability to achieve natural HBV infection in mice, surrogate mouse models are widely used as they have successfully recapitulated many of the cellular and molecular pathogenic and antiviral mechanisms observed during acute and chronic viral hepatitis in humans^{24–29}. Such models include those created either by hydrodynamic injection of a plasmid containing a 1.3-fold overlength HBV genome (pHBV1.3) or a recombinant cccDNA precursor plasmid (prcccDNA) into the tail vein^{30,31}. Alternative models can be established through infection with a recombinant adenovirus expressing HBV (AdHBV) or a recombinant adeno-associated virus serotype 8 expressing HBV (AAV8-HBV)^{32,33}. In these surrogate models, the HBV transcription template is introduced into a proportion of hepatocytes and remains extra-chromosomal, thereby simulating the natural HBV transcription in humans from the cccDNA template. This strategy leads to hepatocyte-specific viral gene expression and replication, driven by authentic HBV promoters and enhancers.

This study investigates how HBsAg is presented to T cells in pre-clinical mouse models. In the liver, the intrahepatic Batf3⁺ XCR1⁺ CCR7⁺ cDC1s present HBsAg to CD8⁺ T cells via MHC-I cross-dressing, while in lymphoid tissues, B cells prime CD4⁺ T cell responses in follicular and interfollicular regions, guided by CCR5 and EBI2. These findings uncover a novel antigen presentation mechanism distinct from classical viral paradigms. The insights gained from these pathways are crucial for advancing innovative vaccines and targeted immunotherapies to better control chronic HBV infection.

Results

Single-cell landscape of T-cell responses in acute HBV patients

A thorough understanding of the T cell responses to HBV infection in patients is limited but crucial to explore potential intercellular mechanisms of HBsAg presentation. To address this question, we conducted single-cell RNA sequencing (scRNA-seq) on peripheral blood mononuclear cells (PBMC) from five patients with acute HBV infection (AHB) and five healthy donors (HD) (Fig. 1a and Supplementary Data 1). This allowed us to examine the transcriptomic profiles of these cells and their T cell receptor (TCR) repertoire (Fig. 1a).

Concurrently, we analyzed immune cells from a liver biopsy of one patient (Fig. 1a). By employing anchoring integration and unsupervised clustering, we identified 36 unique cell types and states (subsets) in a pool of 49,305 high-quality single cells (Fig. 1b), based on their distinct signature markers of gene expression (Supplementary Fig. 1a and Supplementary Data 2). We also confirmed that these cell clusters were consistently present across all PBMC samples (Supplementary Fig. 1b).

We classified the T cells identified among the PBMCs into 18 subsets, including Tfh, effector (TEF), exhausted (TEX) clusters, innate-like T cells, and others (Fig. 1b). By comparing the relative proportions of these subsets in patients and healthy donors, we found the Tfh, cycling CD8⁺, and CD8⁺ TEF granzyme A⁺ (GZMA) subsets were significantly enriched, whereas gamma-delta (γδ) T cells were diminished in patients (Fig. 1c). Gene ontology (GO) pathway enrichment analysis of the T cells further indicated more transcription from genes involved in T cell responses in the cells from patients than in those from healthy donors (Fig. 1d). Moreover, patient TEF and TEX CD8⁺ T cells scored more highly in cytotoxicity assays than did these cells from healthy donors (Fig. 1e). Discriminant regulon expression analysis (DoRothEA), which estimates transcription factor activity from the mRNA levels of their target genes, predicted that the observed enhancement of T cell responses is driven by certain signaling pathways and transcription factors (Supplementary Fig. 1c, d). This includes, but is not limited to, well-known innate immunity modulators such as JAK-STAT signaling pathways, and the transcription factors IRF2 and RELA (Supplementary Fig. 1c, d)^{34,35}, suggesting the presence of a complex regulatory network that influences T cell dynamics. To determine which T cell subsets are involved in the response to acute HBV infection, we analyzed TCR clonality and observed more clonal expansion in patients than in healthy donors (Fig. 1f), particularly expansion of differentiated CD4⁺ T cells, CD8⁺ TEF granzyme K⁺ (GZMK), and CD8⁺ TEF granzyme B⁺ (GZMB) subsets (Fig. 1g). Additionally, we observed an increase in the Vγ9- subset within the γδ T cell population from the PBMCs of acute HBV patients (Supplementary Fig. 1e), consistent with a previous report describing dominant clonal expansions of human Vγ9- T cells during adaptive antiviral immunosurveillance³⁶. These findings indicate a robust T cell response during acute HBV infection.

Myeloid cells are crucial for antigen presentation in T cell immunity¹⁵. These cells comprised 7 subsets within PBMCs, including monocytes, macrophages, and DCs (Fig. 1b). Gene set enrichment (GSEA) and gene expression analyses revealed that, during acute HBV infection, specific subsets of myeloid cells exhibited enhanced activation and adhesion (Fig. 1h and Supplementary Fig. 1f), a response that can be primed by granulocyte-macrophage colony-stimulating factor (GM-CSF)³⁷. In contrast, genes associated with interferon (IFN) production and signaling, as well as pro-inflammatory cytokine secretion, did not show increased expression in these cells compared to those from healthy donors (Fig. 1h and Supplementary Fig. 1f). Additionally, DoRothEA analysis indicated downregulation of key innate immunity modulators, including NF-κB and JAK-STAT signaling pathways, as well as the transcription factor RELA, in these cells (Supplementary Fig. 1g, h). These findings are consistent with previous reports that patients with acute HBV infection do not mount a robust innate immune response to the virus^{6,8}. Further GSEA of DC subsets found that genes involved in lymphocyte activation and immune synapse formation were downregulated in cDC2s from patients when compared with healthy controls (Fig. 1i), suggesting that cDC2s may be ineffective in driving CD4⁺ T cell responses in these patients, contrary of what might be expected from our understanding of classical CD4⁺ T cell activation by cDC2s^{13,21}.

Comparative analysis of the immune cell subsets in PBMCs and matched liver tissue from the same patient revealed significantly greater enrichment of certain myeloid cell and CD8⁺ T cell subsets in the liver than in PBMCs (Supplementary Fig. 1i). By using NicheNet algorithm to predict ligand-receptor interactions between these

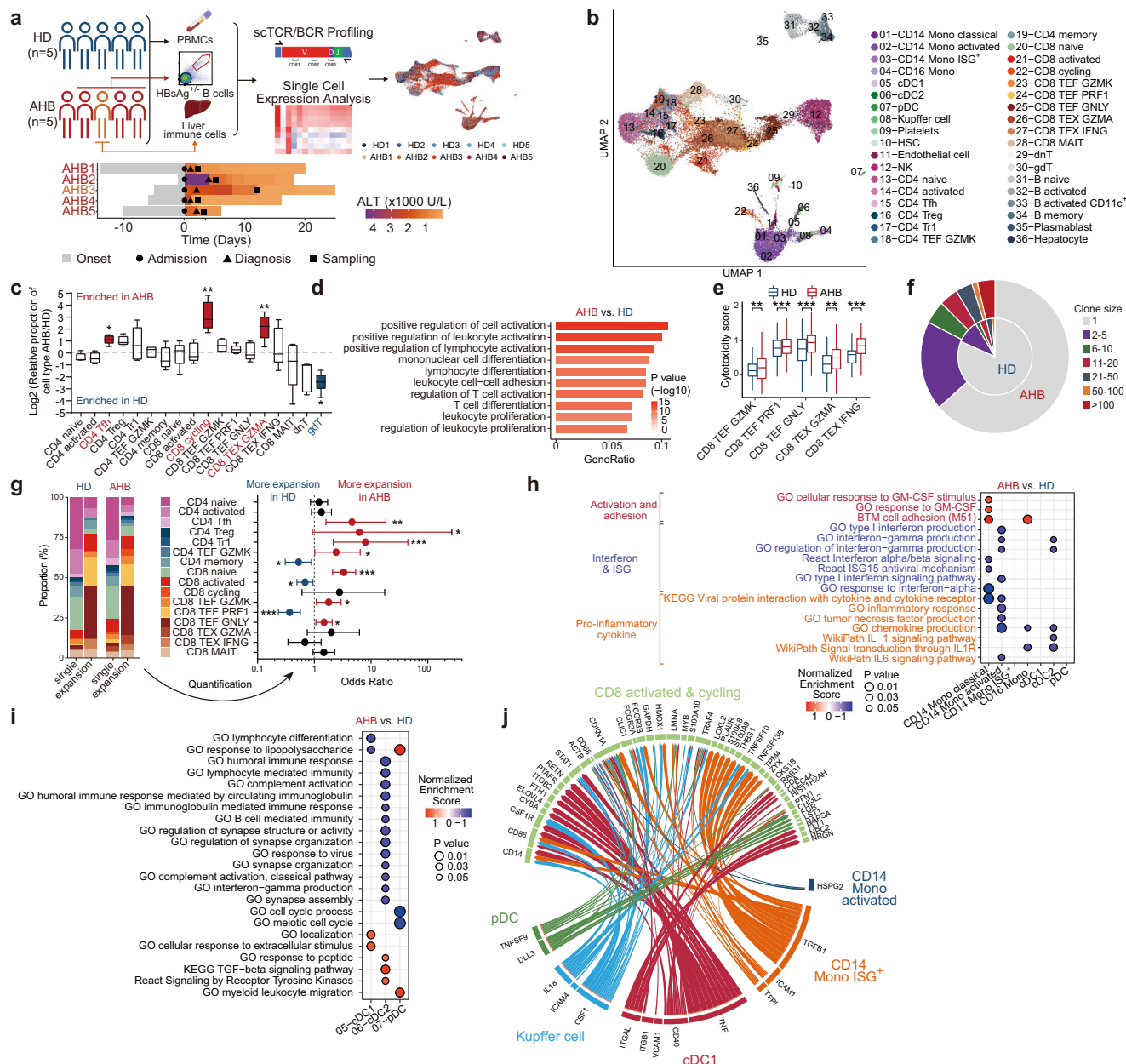


Fig. 1 | Single-cell landscape of T-cell responses in acute HBV patients. a A schematic workflow of the study design (top) and the clinical time course of five acute HBV infection (AHB) patients (bottom) (created with BioRender.com).

b Uniform manifold approximation and projection (UMAP) visualization of PBMCs and liver cells, colored by cluster. CD4 TEF GZMK: Granzyme K⁺ effector CD4⁺ T cells; CD8 TEX GZMA: Granzyme A⁺ exhausted CD8⁺ T cells. **c** Box plots showing the fold enrichment of cell type proportions between AHB patients ($n = 5$) and healthy donors (HDs, $n = 5$). In each plot, the box represents the interquartile range, with the median indicated by a horizontal line. The lower whisker extends to the minimum (lowest value within $1.5 \times \text{IQR}$) and the upper whisker extends to the maximum (highest value within $1.5 \times \text{IQR}$). **d** Pathway enrichment analysis of T cells in AHB patients versus HDs. **e** Box plots illustrating the cytotoxicity scores of TEF and TEX CD8⁺ T cell subsets in AHB patients ($n = 5$) versus HDs ($n = 5$). Each box plot displays the minimum, lower quartile, median, upper quartile, and maximum

values. **f** Clonal status percentages of T cells across AHB patients and HDs.

g Proportion of single and expanded clones (left) and quantification of clonal expansion (right) in T cell clusters in AHB patients ($n = 5$) versus HDs ($n = 5$). The point estimates (odds ratios) are depicted with error bars representing the 95% confidence intervals. **h** Gene set enrichment analysis (GSEA) of myeloid cell clusters in AHB patients versus HDs. ISG: Interferon-stimulated genes. **i** GSEA of dendritic cells (DCs) in AHB patients versus HDs. **j** Circos plot illustrating the prioritized interactions mediated by ligand-receptor pairs between hepatic-enriched myeloid cell subsets and activated and cycling CD8⁺ T cells within the liver. Statistical analysis was performed using two-tailed Mann-Whitney tests (c), one-tailed Fisher's exact test (d), two-tailed Student's t -tests (e), two-tailed Fisher's exact test (g) and Kolmogorov-Smirnov (K-S) test followed by Benjamini-Hochberg procedure (h, i). Statistically significant results are labeled (* $p < 0.05$, ** $p < 0.01$, *** $p < 0.001$).

enriched cell subsets, we found that cDC1s established most ligand-receptor interactions with activated and proliferating CD8⁺ T cells, surpassing even the interactions of Kupffer cells (specialized macrophages in the liver) and other myeloid cells with CD8⁺ T cells (Fig. 1j). This suggests that cDC1s, in addition to the previously reported Kupffer cells^{38–40}, may be also crucial for priming CD8⁺ T cell responses

against HBV in the liver, though further in-depth studies involving more patients are needed to confirm these findings. Overall, our scRNA-seq analysis indicates that HBsAg presentation underlying T cell immunity in acute HBV patients may involve cDC1s, independent of cDC2s, suggesting the potential presence of novel intercellular mechanisms.

Intrahepatic Batf3⁺XCRI⁺CCR7⁺ cDC1s drive CD8⁺ T cell response against HBsAg

As the location of CD8⁺ T cell priming in HBV infection remains poorly understood⁵, we began investigating the sites of CD8⁺ T cell responses following HBsAg expression in hepatocytes. To do so, we created a recombinant HBV construct, pHBV1.3/ovalbumin (OVA) 257-264, which expresses HBsAg fused to an epitope of OVA, OVA257-264, in the context of HBV replication (Supplementary Fig. 2a). This epitope is recognized specifically by the CD8⁺ T cells of OT-I mice, which express a transgenic TCR specific for the OVA257-264 peptide bound to the MHC-I molecule H-2K^b⁴¹. The recombinant HBsAg, containing the inserted epitope, remains functional: it is secreted and supports HBV release (Supplementary Fig. 2b). Also, it has a buoyant density and particle size similar to wild-type (WT) HBsAg (Supplementary Fig. 2c, d). Following hydrodynamic injection into the tail vein of mice (Supplementary Fig. 2e), this construct instigated earlier activation, increased division, and amplified effector functions of OT-I T cells in the liver than in the spleen and liver-dLNs, as analyzed by flow cytometry (Supplementary Fig. 2f). Consistent with this conclusion, the CD8⁺ T cell response in the liver was unchanged by prior splenectomy combined with an anti-CD62L antibody treatment (Supplementary Fig. 2g, h), which inhibits the homing of naïve T cells to LNs, or treatment with sphingosine-1-phosphate receptor modulator FTY720 (Supplementary Fig. 2g, i), which blocks the egress of T cells from LNs. We further confirmed that the liver supports CD8⁺ T cell responses against HBsAg using HBV Env28 TCR transgenic T cells (Supplementary Fig. 2e, j), which specifically recognize an HBsAg epitope presented by MHC-I (H-2K^b)⁴². These results corroborate the essential role of the liver in priming CD8⁺ T cells against HBsAg, at least in mice^{42,43}.

The mechanism of CD8⁺ T cell priming in the liver is controversial due to the multiplicity and heterogeneity of antigen-presenting cells^{38–40,44}. To identify the subsets and the cellular interaction responsible for HBsAg-related CD8⁺ T cell responses in the liver, we performed scRNA-seq on liver cells sorted by fluorescence activated cell sorting (FACS) from mice at days 0 and 2.5 after the hydrodynamic injection of pHBV1.3/OVA257-264 (Supplementary Fig. 3a). This analysis identified various cell types, including diverse DC and CD8⁺ T cell subsets in the liver (Fig. 2a, b, Supplementary Fig. 3b and Supplementary Data 3), with clustering patterns similar to those observed in humans (Fig. 1b)⁴⁵. We analyzed the subsets for the presence of MHC-I (H-2K^b) molecules bound to the OVA257-264 peptide epitope SIINFEKL by flow cytometry after labeling with an antibody, 25-D1.16, which binds specifically to the H-2K^b-SIINFEKL complex. Intrahepatic resident cDC1s (CCR7⁺) had the most H-2K^b-SIINFEKL complex, hepatocytes, LSECs, migratory cDCs (CCR7⁺, mig-cDCs), and monocyte-derived DCs (mono-DCs) had lesser amounts, and Kupffer cells, B cells and cDC2s had none (Fig. 2c). Co-culture of OT-I T cells with various liver cell subsets showed that only cDC1s could induce OT-I T cell proliferation (Fig. 2d). Consistent with this finding, 3.5 days after hydrodynamic injection, OT-I T cell proliferation and differentiation were nearly completely blocked in Batf3 KO mice (Fig. 2e, f), which lack cDC1s in their liver (Supplementary Fig. 3c). Furthermore, when the recruitment of cDC1 cells via the XCRI receptor and its ligand XCL1 was blocked using an anti-XCL1 antibody, there was significantly less OT-I T cell proliferation and differentiation (Fig. 2g, h). By contrast, OT-I T cell proliferation and differentiation were unaffected in monocyte-deficient CCR2 KO, Kupffer cell-depleted, and B cell-deficient μ MT mice (Supplementary Fig. 3d–i). We conclude from these experiments that the intrahepatic resident Batf3⁺XCRI⁺CCR7⁺ cDC1s are the subset of antigen-presenting cells crucial for HBsAg-specific CD8⁺ T cell responses in the liver, aligning with the established role of cDC1s in CD8⁺ T cell responses^{13,46}, as exemplified by lymphocytic choriomeningitis virus (LCMV) Armstrong infection (Supplementary Fig. 3j, k).

We confirmed our conclusion that the cDC1s initiate CD8⁺ T cell responses against HBsAg by using HBV Env28 TCR transgenic T cells

(Fig. 2i, j). Further validation was provided by employing an MHC-peptide tetramer and 5-ethynyl-2'-deoxyuridine (EdU) incorporation assay to detect the proliferation of endogenous HBsAg-specific CD8⁺ T cells (Fig. 2k, l), thereby ruling out the potential artifact associated with transgenic TCRs. The predominance of cDC1s in the CD8⁺ T cell response in the liver was also evident in two additional HBV mouse models: the prccDNA model (Supplementary Fig. 3l, m) and the AdHBV model with a high infection dose of 3×10^9 infectious units (i.u.) (Supplementary Fig. 3n, o)³². In addition, supporting a specific role of cDC1s in HBsAg presentation, we found that cDC1s (Fig. 2m, and Supplementary Fig. 4a, b), but not macrophages (Supplementary Fig. 4c), were essential for the clearance of HBsAg from liver tissues. Thus, consistent with the NicheNet analysis of our human scRNA-seq data (Fig. 1j), the intrahepatic resident Batf3⁺XCRI⁺CCR7⁺ cDC1s are the primary antigen-presenting cells in the CD8⁺ T cell response against HBsAg in the liver.

The cDC1s acquire and present HBsAg by MHC-I cross-dressing but not cross-presentation

cDC1s can present the antigens that they take up by endocytosis on MHC-I rather than on MHC-II molecules, a process called cross-presentation⁴⁶. To investigate whether cDC1s elicit CD8⁺ T cell responses to HBsAg by endocytosis and cross-presentation, we first tested whether a non-secreted variant of recombinant HBsAg expressed by the pHBV1.3/OVA257-264 construct would prime the OT-I T cell response. Despite the fact that this form of recombinant HBsAg was not secreted (Supplementary Fig. 5a), the amount of MHC-I-SIINFEKL on cDC1s and the OT-I T cell response was unaffected after hydrodynamic injection of this construct into WT mice that had previously received a transfer of OT-I T cells (Supplementary Fig. 5b–d), indicating that cDC1s do not take up recombinant HBsAg by endocytosis for cross-presentation. We investigated whether cDC1s take up recombinant HBsAg released from hepatocytes in extracellular vesicles (exosomes) by using Rab27a KO mice in which exosome release is impaired^{47,48}. Again, MHC-I-SIINFEKL presentation and OT-I T cell responses were unaffected (Supplementary Fig. 5e–g). Also, we examined whether cDC1s acquired HBsAg from dying hepatocytes by expressing HBsAg as a fluorescent fusion protein with ZsGreen from an HBV replicon, utilizing the virus's own hepatocyte-specific promoter (Supplementary Fig. 5h). The ZsGreen signal in hepatocytes indicated intracellular HBsAg (Supplementary Fig. 5i). Although we found ZsGreen in Kupffer cells and liver sinusoidal endothelial cells (LSEC), we did not find it in cDC1s (Supplementary Fig. 5j). Furthermore, blocking DNDR-1, a receptor implicated in dead cell debris recognition and internalization by cDC1s⁴⁹, did not affect antigen presentation or CD8⁺ T cell priming by cDC1s (Supplementary Fig. 5k–m). Together, these data indicate that the Batf3⁺XCRI⁺CCR7⁺ cDC1s do not acquire recombinant HBsAg from the environment, thus they may not use classical cross-presentation to present on MHC-I-HBsAg peptide antigens to CD8⁺ T cells.

cDC1s can acquire antigenic peptides bound to MHC-I by non-canonical MHC-I cross-dressing under certain circumstances⁵⁰. If the Batf3⁺XCRI⁺CCR7⁺ cDC1s obtain intact HBsAg peptide-MHC-I complexes from neighboring cells by MHC-I cross-dressing, MHC-I expression by the cDC1s would not be necessary for a T cell response. To test this prediction, we transferred cDC1s from MHC-I-deficient β 2M KO mice, or control WT mice, into cDC1-deficient Batf3 KO mice (Fig. 3a). Unlike in LCMV Armstrong infection, where MHC-I expression on cDC1s was required for effective CD8⁺ T cell priming by cross-presentation (Supplementary Fig. 6a, b), the β 2M KO cDC1s primed CD8⁺ T cell responses against HBsAg as well as the WT cDC1s did, indicating that the MHC-I defective cDC1s acquired HBsAg peptide-MHC-I complexes from neighboring cells by cross-dressing (Fig. 3b, c). To consolidate this conclusion, we implanted bone marrow from Batf3 KO or WT BALB/c (H-2K^d) into lethally irradiated F1 (C57BL/

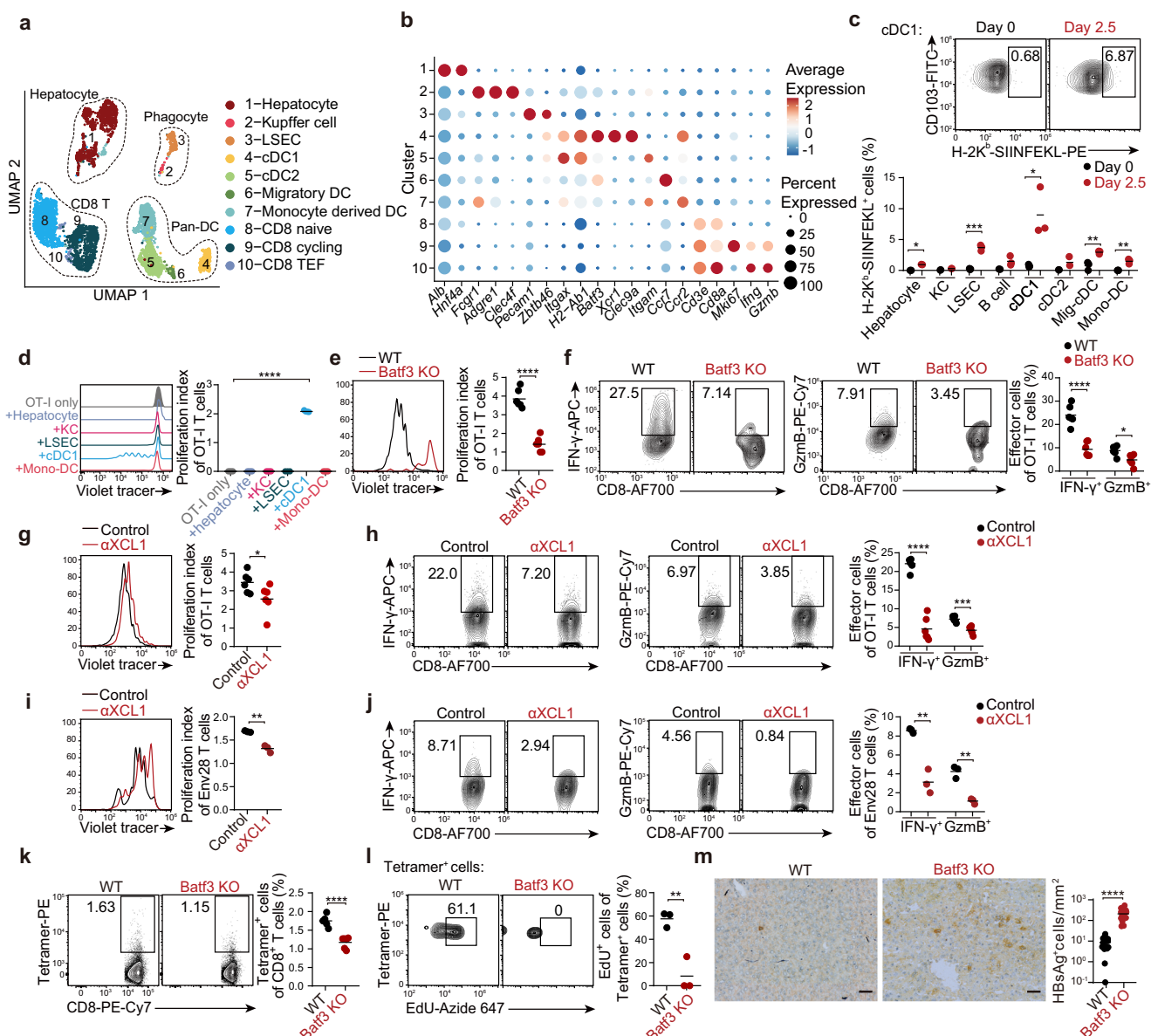


Fig. 2 | Intrahepatic Batf3⁺XCRI⁺CCR7⁺ cDC1s drive CD8⁺ T cell response against HBsAg. **a** UMAP plot of 4829 single liver cells as illustrated in Supplementary Fig. 3a. **b** Dot plot of selected canonical cell markers across populations detailed in (a). **c** Representative FACS plots and percentages of H-2K^b-SIINFEKL-expressing antigen-presenting cells (APCs) in WT mouse livers at days 0 and 2.5 post-pHBV1.3/OVA257-264 hydrodynamic injection (HDI) ($n = 3$). **d** Representative Violet tracer dilution and proliferation index of OT-I T cells after a 3-day culture alone or with liver-sorted APCs from WT mice post-1 day pHBV1.3/OVA257-264 HDI ($n = 6$ biologically independent replicates). **e, f** Violet tracer-labeled OT-I T cells were transferred into WT or Batf3 KO mice, followed by pHBV1.3/OVA257-264 HDI for 3.5 days. **e** Representative Violet tracer dilution and proliferation index ($n = 6$). **f** Representative FACS plots and percentages of IFN- γ ⁺ or GzmB⁺ OT-I T cells ($n = 6$). **g, h** Violet tracer-labeled OT-I T cells were transferred into WT recipients treated with anti-XCL1 versus control antibody, followed by pHBV1.3/OVA257-264 HDI for

3.5 days. **g** Representative Violet tracer dilution and proliferation index ($n = 6$). **h** Representative FACS plots and percentages of IFN- γ ⁺ or GzmB⁺ OT-I T cells ($n = 6$). **i, j** Same as (g, h) but using HBV Env28 T cells as donors and BALB/C mice as recipients receiving pHBV1.3 for HDI ($n = 3$). **k, l** Representative FACS plots and percentages of HBV ENV353 tetramer-specific CD8⁺ T cells in Batf3 KO versus WT mice at day 5 post-pHBV1.3 HDI ($n = 6$), and representative FACS plots and percentages of EdU⁺ cells among these tetramer-specific CD8⁺ T cells ($n = 3$). **m** Intrahepatic HBsAg levels in WT and Batf3 KO mice on day 14 post-pHBV1.3 HDI ($n = 15$ fields from 5 mice). Scale bars, 50 μ m. At least two independent experiments were performed. The horizontal lines represent median values. Statistical significance was calculated using one-way ANOVA with Dunnett's multiple comparisons test (d) and two-tailed Student's *t*-tests (c, e-m). Significance levels are indicated as follows: * $p < 0.05$, ** $p < 0.01$, *** $p < 0.001$, **** $p < 0.0001$. Source data and exact *p*-values are provided in the Source Data file.

6 X BALB/c) mice (Fig. 3d). Upon pHBV1.3/OVA257-264 injection, OT-I T cell expansion occurred in chimeras reconstituted with BALB/c bone marrow, but not in those with Batf3 KO bone marrow (Fig. 3e), underscoring H-2K^b-restricted OT-I response mediated by BALB/c cDC1s. The cDC1s in the mice that received the BALB/c bone marrow were exclusively BALB/c-derived, as expected (Supplementary Fig. 6c). When we measured the percentages of various classes of BALB/c DCs that had H-2K^b-SIINFEKL, the class with the highest percentage was the

cDC1s (Fig. 3f), indicating that these cells must have acquired the H-2K^b-SIINFEKL by cross-dressing.

To demonstrate that MHC-I cross-dressing was not confined to a specific experimental system, we first confirmed that the response of endogenous HBsAg-specific CD8⁺ T cells was independent of MHC-I expression on cDC1s in the pHBV1.3 mouse model (Fig. 3g). Further, by reconstituting F1 mice with either Batf3 KO or C57BL/6 (H-2K^b) bone marrow, we showed that C57BL/6-derived cDC1s could also mediate

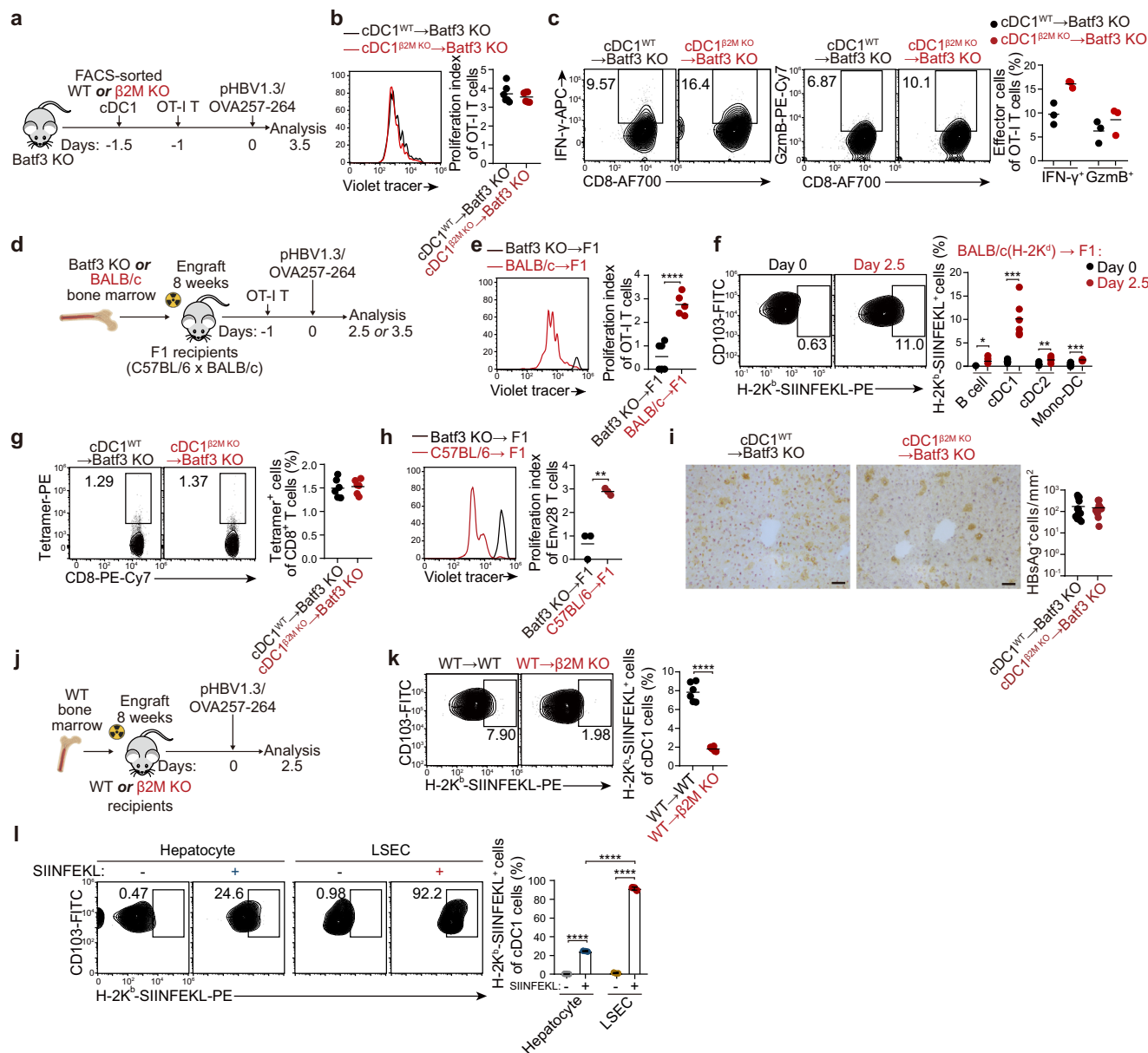


Fig. 3 | The cDC1s acquire and present HBsAg by MHC-I cross-dressing. **a** A schematic of the cell reconstitution strategy and experimental timeline. **b** Representative Violet tracer dilution and proliferation index from the mice described in (**a**) ($n = 6$). **c** Representative FACS plots and percentages of IFN- γ ⁺ or GzmB⁺ OT-I T cells from the mice described in (**a**) ($n = 3$). **d** Schematic of bone marrow chimeras generation and experimental timeline (created with BioRender.com). **e** Representative Violet tracer dilution and proliferation index of OT-I T cells from mice described in (**d**) at day 3.5 post-pHBV1.3/OVA257-264 HDI ($n = 5$). **f** Representative FACS plots and percentages of H-2K^b-SIINFEKL-expressing BALB/c APCs at day 0 and 2.5 in the livers of mice from (**d**) post-pHBV1.3/OVA257-264 HDI ($n = 6$). **g** Representative FACS plots and percentages of ENV353 tetramer-specific CD8⁺ T cells from mice described in (**a**) at day 5 post-pHBV1.3 HDI ($n = 6$). **h** Representative Violet tracer dilution and proliferation index of Env28 T cells in F1 chimeras reconstituted with C57BL/6 versus Batf3 KO bone marrow at day 3.5 post-

pHBV1.3 HDI ($n = 3$). **i** Intrahepatic HBsAg levels in Batf3 KO mice reconstituted with β 2M KO or WT cDC1s at day 14 post-pHBV1.3 HDI ($n = 15$ view fields from 5 mice). Scale bars, 50 μ m. **j** Schematic of chimeras generation and experimental timeline (created with BioRender.com). **k** Representative FACS plots and percentages of H-2K^b-SIINFEKL-expressing cDC1s from mice described in (**j**) at day 2.5 post-pHBV1.3/OVA257-264 HDI ($n = 6$). **l** Representative FACS plots and percentages of H-2K^b-SIINFEKL-expressing cDC1s after a 1-day co-culture with unpulsed or SIINFEKL-pulsed hepatocytes or LSECs ($n = 3$ biologically independent replicates). At least two independent experiments were performed. Horizontal lines in (**b**, **c**, **e**–**i**, **k**) represent median values. Error bars in (**l**) represent mean \pm SD. Statistical significance was calculated using two-tailed Student's t -tests (**b**, **c**, **e**–**i**, **k**) and one-way ANOVA with Tukey's multiple comparisons test (**l**). Significance levels are indicated as follows: $^*p < 0.05$, $^{**}p < 0.01$, $^{***}p < 0.001$, $^{****}p < 0.0001$. Source data and exact p -values are provided in the Source Data file.

the H-2K^d-restricted response of HBV Env28 TCR transgenic T cells (Fig. 3h). Similar evidence of cDC1 cross-dressing was observed in both the prcccDNA and high-dose AdHBV models. Specifically, HBsAg-specific CD8⁺ T cell expansion occurred independently of MHC-I expression on cDC1s (Supplementary Fig. 6d, e), and C57BL/6-derived cDC1s mediated the H-2K^d-restricted response of HBV Env28 TCR transgenic T cells in these two models (Supplementary Fig. 6f, g). cDC1

cross-dressing was also observed after hydrodynamic injection of a low dose of pHBV1.3/OVA257-264 (Supplementary Fig. 7a–c), which resulted in low HBsAg expression (Supplementary Fig. 7d, e), and in AdHBV (low-dose infection: 1×10^8 i.u.³²) and AAV8-HBV infections (Supplementary Fig. 7f–k), both of which caused mild yet observable liver inflammation (Supplementary Fig. 7l)^{32,31}. These findings suggest that cDC1 cross-dressing may not be exclusively dependent on the

rapid expression of a large amount of HBsAg or on marked inflammation. Moreover, hydrodynamic injection of the pALB-Igk/HEL-OVA257-264 plasmid, expressing a secreted hen egg lysozyme (HEL)-OVA257-264 fusion protein under the hepatocyte-specific albumin (ALB) promoter (Supplementary Fig. 8a), demonstrated that cDC1s drove OT-I T cell proliferation in a manner dependent on the expression of MHC-I by cDC1s themselves (Supplementary Fig. 8b, c). This raises the possibility that cDC1 cross-dressing may not be a general feature of secreted proteins from hepatocytes, but rather a mechanism potentially specific to HBsAg. Finally, while cDC1s played a significant role in intrahepatic HBsAg clearance (Fig. 2m and Supplementary Fig. 4a, b), this process did not require MHC-I expression by cDC1s (Fig. 3i), indicating that MHC-I cross-dressing of cDC1s contributes to the clearance of intrahepatic HBsAg. In conclusion, intrahepatic resident Batf3⁺XCRI⁺CCR7⁺ cDC1s drive the CD8⁺ T cell response against HBsAg in the liver through MHC-I cross-dressing.

Irradiation-resistant cells provide HBsAg peptide-MHC-I complexes for cross-dressing

To identify the source of HBsAg peptide-MHC-I complexes for cross-dressing of cDC1s, we reconstituted irradiated WT and β 2M KO mice with bone marrow from WT mice (Fig. 3j). Many fewer cDC1s presented recombinant HBsAg in the β 2M KO mice when compared with the WT controls (Fig. 3k), suggesting that the HBsAg peptide-MHC-I complexes used to cross-dress cDC1s come from irradiation-resistant cells. LSECs, which can uptake dying hepatocytes (Supplementary Fig. 5j), present H-2K^b-SIINFEKL complexes at higher levels than hepatocytes (Fig. 2c). This led us to hypothesize that LSECs, in addition to HBsAg-producing hepatocytes, may contribute to cross-dressing of cDC1s. To test this, we loaded SIINFEKL onto both LSECs and hepatocytes and cocultured them with cDC1s to assess H-2K^b-SIINFEKL complex transfer. Flow cytometry analysis showed that both LSECs and hepatocytes transferred these complexes to cDC1s, with LSECs demonstrating greater efficiency (Fig. 3l). In conclusion, intrahepatic resident Batf3⁺XCRI⁺CCR7⁺ cDC1s likely utilize HBsAg peptide-MHC-I complexes derived from irradiation-resistant cells, particularly LSECs, to drive the CD8⁺ T cell response against HBsAg.

B cells but not cDCs initiate CD4⁺ T cell responses against HBsAg

To investigate the mechanism by which antigen-presenting cells acquire HBsAg to drive CD4⁺ T cell responses, we generated a recombinant pHBV1.3 replicon (pHBV1.3/OVA323-339) that expresses HBsAg fused to the OVA323-339 peptide (Supplementary Fig. 2a). The OVA323-339 peptide bound to MHC-II is recognized by CD4⁺ T cells in OT-II mice, analogous to the previous CD8⁺ T cell experiments with OT-I mice. To identify the antigen-presenting cell subsets that present OVA323-339 to CD4⁺ T cells, we transferred OT-II T cells into mice lacking one subset and then introduced pHBV1.3/OVA323-339 by hydrodynamic injection. Ablation of all cDCs in Zbtb46-diphtheria toxin (DT) receptor (DTR) mice by treatment with the toxin had no effect on early OT-II T cell activation (Supplementary Fig. 9a), proliferation (Supplementary Fig. 9b), or Tfh and effector differentiation (Supplementary Fig. 9c, d) in the spleen, dLNs, and liver after injection of pHBV1.3/OVA323-339, as determined by flow cytometry. This was true, likewise, when either the cDC1 or the cDC2 subset was constitutively deficient in Batf3 KO mice and *Irf4*^{fl/fl}CD11cCre mice, respectively (Supplementary Fig. 9e, f). As a positive control, immunization with OVA-conjugated sheep red blood cells (SRBC-OVA) elicited the classical cDC-dependent OT-II T cell responses (Supplementary Fig. 9g, h)⁵². These findings challenge the conventional paradigm that cDCs, especially cDC2s, initiate CD4⁺ T cell responses^{13,21}, but are consistent with our human scRNA-seq data (Fig. 1i) and with the clearance of intact HBsAg from the circulation and liver tissues in *Irf4*^{fl/fl}CD11cCre mice (Supplementary Fig. 10a, b).

Similarly, the absence of monocytes or macrophages had no effect on OT-II T cell proliferation (Supplementary Fig. 9i, j). In B cell-

deficient μ MT mice, by contrast, OT-II T cell activation was abrogated in the spleen and impaired in the dLNs but remained intact in the liver (Fig. 4a). Notably, there was almost no proliferation (Fig. 4b) or differentiation (Fig. 4c, d) of OT-II T cells in these three organs of μ MT mice. These findings indicate that B cells are essential for initiating OT-II T cell responses, though other cells may provide weak activation signals that are insufficient for full responses, particularly in the liver. A similar phenomenon was observed in vesicular stomatitis virus (VSV)-specific BCR transgenic VIIIOYEN mice (Supplementary Fig. 11a-c), which lack a normal B cell repertoire. Importantly, a role of B cells was also observed in the response of endogenous CD4⁺ T cells, which differentiated less in μ MT mice than in WT mice (Fig. 4e, f), whereas they differentiated normally in cDC-ablated mice (Supplementary Fig. 9k, l). The essential role of B cells in initiating endogenous CD4⁺ T cell responses to HBsAg was also demonstrated in both the prcccDNA and high-dose AdHBV mouse models (Supplementary Fig. 11d-g). Additionally, B cells initiated CD4⁺ T cell responses under low HBsAg expression induced by hydrodynamic injection of a low dose of pHBV1.3/OVA323-339 (Supplementary Fig. 12a), or during mild inflammation in low-dose AdHBV and in AAV8-HBV infections (Supplementary Fig. 12b-e). Moreover, the lack of MHC-II on B cells (Fig. 4g), but not on phagocytes (Supplementary Fig. 9m), significantly impeded OT-II T cell proliferation, suggesting that B cells prime CD4⁺ T cell responses against recombinant HBsAg by presenting antigens on MHC-II. Finally, B cells contributed to the clearance of both circulating and intrahepatic HBsAg (Fig. 4h, i), as did CD4⁺ T cells (Supplementary Fig. 13a, b). However, injection of the mouse HBsAg-specific monoclonal antibody 129G1⁵³ resulted in the clearance of only circulating HBsAg, without affecting intrahepatic HBsAg clearance (Supplementary Fig. 13c, d). These findings suggest that B cells may not only mediate an antibody response, with the assistance of Tfh cells, to clear circulating HBsAg, but also initiate effector CD4⁺ T cell responses to clear intrahepatic HBsAg. Thus, B cells are the principal antigen-presenting cells that initiate CD4⁺ T cell responses against HBsAg.

B cells acquire nonopsonized HBsAg in situ

To study where and how HBsAg-specific B cells acquire HBsAg for initiating CD4⁺ T cell responses, we developed a knock-in mouse model, termed S129G1_{HL}, that expresses a monoallelic immunoglobulin (Ig) heavy/light chain derived from the 129G1 monoclonal antibody⁵³, along with a human Igk constant region (HuCk) (Fig. 5a). B cells in these mice predominantly expressed the engineered B cell receptor, which recognizes HBsAg (Fig. 5b). We transferred S129G1_{HL} B cells into congenic WT mice and blocked the entry of patrolling B cells into the white pulp (lymphoid region) of the spleen by using anti-LFA-1 and anti- α 4 antibodies⁵⁴, and into LNs by using an anti-CD62L antibody, respectively (Fig. 5c). Following the blockade and 18 hours after pHBV1.3 injection, we observed that the BCR signaling intensity, as indicated by Nur77 expression, remained intact in S129G1_{HL} B cells from both the spleen and dLNs (Fig. 5d, e), suggesting that S129G1_{HL} B cells can acquire HBsAg in the white pulp of the spleen and dLNs without the need for patrolling the periphery. Likewise, splenectomy and B cell egress inhibition from LNs using FTY720 also did not alter S129G1_{HL} B cell activation in the liver (Fig. 5f), suggesting that S129G1_{HL} B cell antigen engagement in the liver is independent of the spleen and dLNs. Furthermore, 18 hours after pHBV1.3 injection, the S129G1_{HL} B cells had not migrated to outer B cell follicles near antigen-rich areas like the marginal or subcapsular sinus (Fig. 5g)¹⁷, indicating that S129G1_{HL} B cells acquire HBsAg in situ.

Once antigens are passively transported to the lymphoid tissues via blood or lymph, small, soluble antigens with a radius of less than approximately 5.5 nm (about 70 kDa) can filter through the conduit system to gain direct access to lymphoid B cell follicles¹⁴, while larger antigens require active transport by accessory or resident cells after opsonization to gain access to these follicles¹⁷. Complement

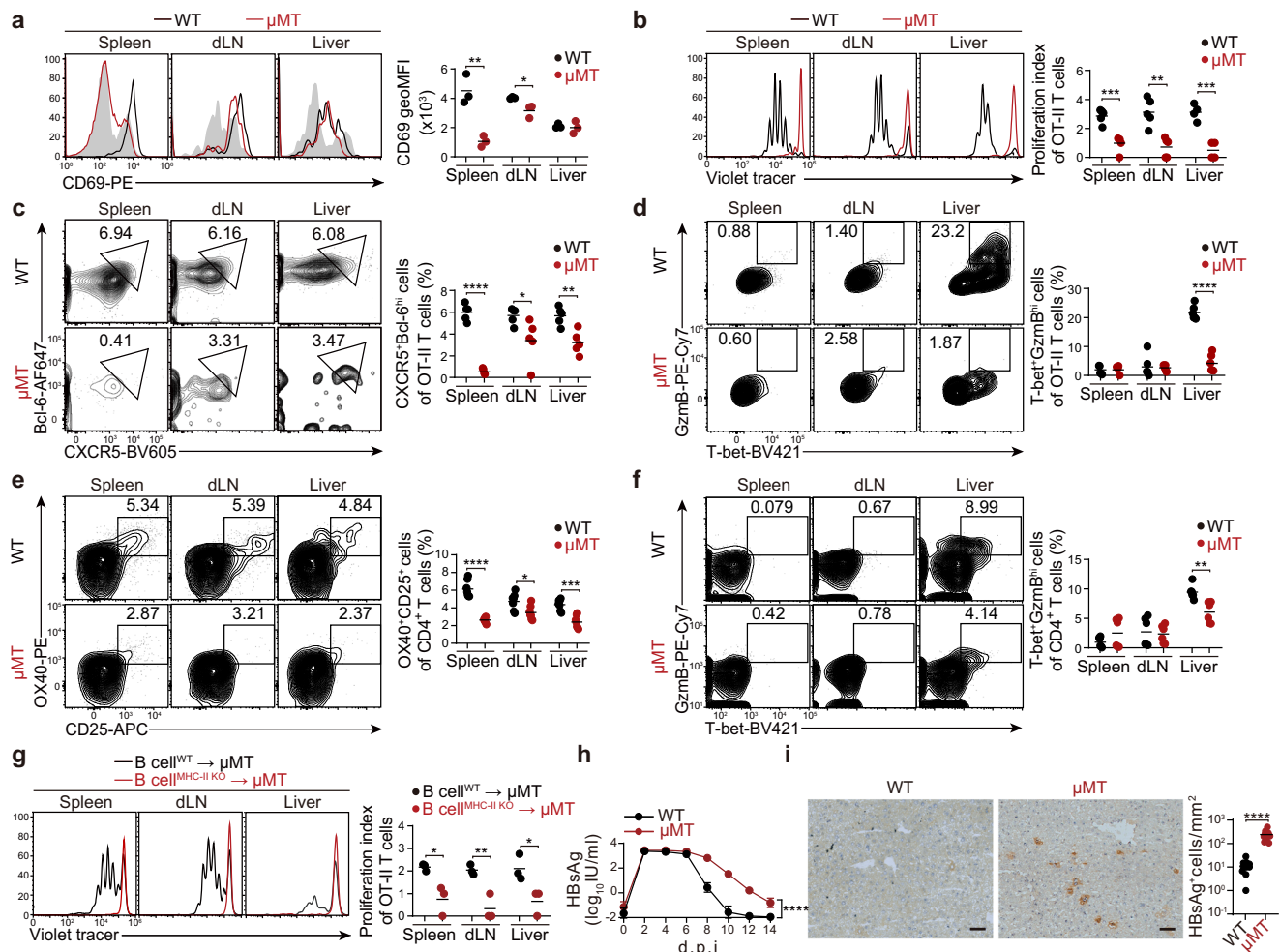


Fig. 4 | B cells initiate CD4⁺ T cell responses against HBsAg. **a–d** OT-II T cells, labeled with Violet tracer where indicated, were transferred into WT or μMT mice, followed by pHBV1.3/OVA323-339 HDI. Spleens, draining LNs (dLNs), and livers were harvested for FACS analysis from days 2 to 4.5 post-HDI. **a** Representative histogram and geoMFI data of CD69 expression at day 2 ($n = 3$). **b** Representative Violet tracer dilution and proliferation index at day 3.5 (spleen and dLN: $n = 5$; liver: $n = 4$). **c** Representative FACS plots and percentages of CXCR5⁺Bcl6^{hi} OT-II T cells at day 3.5 ($n = 5$). **d** Representative FACS plots and percentages of T-bet⁺Gzmb^{hi} OT-II T cells at day 4.5 ($n = 6$). **e, f** Representative FACS plots and percentages of endogenous CD25⁺OX40⁺ (**e**, $n = 7$) and T-bet⁺Gzmb^{hi} (**f**, $n = 6$) CD4⁺ T cells in the spleens, dLNs, and livers from μMT versus WT mice at day 5 post-pHBV1.3 HDI.

g Representative Violet tracer dilution and proliferation index of transferred OT-II T cells in spleens, dLNs, and livers from μMT mice reconstituted with MHC-II KO versus WT B cells at day 3.5 post-pHBV1.3/OVA323-339 HDI ($n = 3$). **h, i** Circulating HBsAg levels (**h**, $n = 4$) and intrahepatic HBsAg levels (**i**, $n = 15$ view fields from 5 mice) in WT and μMT mice, with serum collected at the indicated time point and liver tissues on day 14 after pHBV1.3 HDI. Scale bars, 50 μm. At least two independent experiments were performed. Horizontal lines in (**a–g**, **i**) represent median values. Error bars in (**h**) show mean ± SD. Statistical significance was calculated using two-tailed Student's *t*-tests (**a–g**, **i**) and two-way ANOVA (**h**). Significance levels are indicated as follows: * $p < 0.05$, ** $p < 0.01$, *** $p < 0.001$, **** $p < 0.0001$. Source data and exact *p*-values are provided in the Source Data file.

component 3 (C3) and Fc-gamma receptor IIB (FcγRIIB) are essential for antigen opsonization¹⁷. Supporting this model, the small soluble HEL protein (approximately 14.4 kDa) expressed via hydrodynamic injection of the pALB-Igk/HEL plasmid, induced intact BCR signaling in HEL-specific Hy10 B cells after knockout of C3 or FcγRIIB expression (Supplementary Fig. 14a, b), or depletion of cDCs or macrophages (Supplementary Fig. 14c, d). Surprisingly, HBsAg, despite being a large subviral particle far exceeding 70 kDa in size, similarly did not require the expression of C3, FcγRIIB, or the involvement of cDCs or macrophages to elicit BCR signaling in S129G1_{HL} B cells following pHBV1.3 injection (Fig. 5h–k). Importantly, HBsAg's ability to bypass these factors is not due to a lack of HBsAg-specific antibodies for opsonization. Natural IgG binding to HBsAg was detectable in WT but absent in B cell-deficient μMT mice (Supplementary Fig. 14e). Furthermore, HBsAg-specific IgG was induced as early as 18 hours after hydrodynamic injection of pHBV1.3 in WT mice (Supplementary Fig. 14f). These findings indicate that HBsAg can reach lymphoid B cell follicles without undergoing the opsonization process or being constrained by the

conduit system's size limitations, thereby enabling S129G1_{HL} B cells to acquire HBsAg in situ, challenging established assumptions^{14,17}.

B cells initiate CD4⁺ T cell responses sequentially in follicular and interfollicular areas

To examine where HBsAg-specific B cells present antigen to their cognate CD4⁺ T cells, we followed the migration of S129G1_{HL} B cells and OT-II T cells in WT recipients by immunofluorescence microscopy after injection of pHBV1.3/OVA323-339. After 24 hours, around half of the OT-II T cells had migrated from the T cell zone to follicular regions of the spleen and dLNs (Fig. 6a, b), some of which co-localized with S129G1_{HL} B cells. When non-cognate V10YEN B cells and OT-II T cells were transferred into HEL-specific BCR transgenic MD4 mice, by contrast, the T cells neither migrated into follicles (Supplementary Fig. 15a, b) nor were activated (Supplementary Fig. 15c). Thus, T cell migration into follicles appears to depend on cognate B cells. After 1.5 days, both S129G1_{HL} B and OT-II T cells began to accumulate in the interfollicular regions between the follicles and remained enriched in

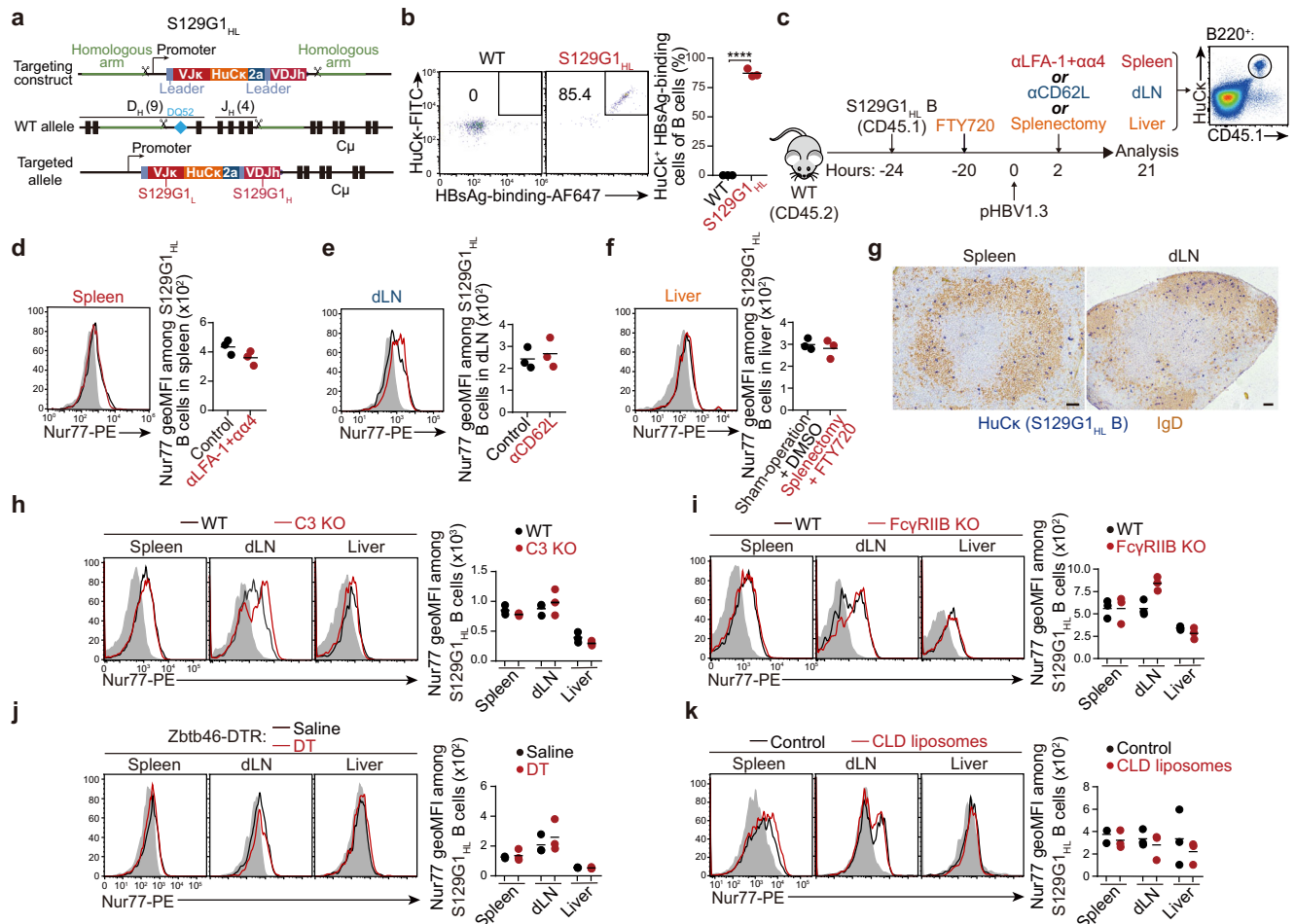


Fig. 5 | B cells acquire nonopsonized HBsAg in situ. **a** Schematic illustrating the targeting strategy for generating HBsAg-specific Ig knock-in mice, named S129G1_{HL}. **b** Representative FACS plots and percentages of HuCk⁺, HBsAg-binding cells in the blood from S129G1_{HL} versus WT mice, gated on B220⁺ cells ($n = 3$). **c** Schematic showing the time course of the B cell response to HBsAg. **d** Representative histograms and geoMFI data of Nur77 expression in S129G1_{HL} B cells in the spleens from WT recipients treated with both anti-LFA-1 and anti- $\alpha 4$ versus control antibodies, at 21 hours post-pHBV1.3 HDI ($n = 3$). **e** Representative histograms and geoMFI data of Nur77 expression in S129G1_{HL} B cells in the dLNs from WT recipients treated with anti-CD62L versus control antibodies, at 21 hours post-pHBV1.3 HDI ($n = 3$). **f** Representative histograms and geoMFI data of Nur77 expression in the livers from mice with both splenectomy and FTY720 versus control treatments, at 21 hours post-pHBV1.3 HDI ($n = 3$).

post-pHBV1.3 HDI ($n = 3$). **g** Immunohistochemistry of spleens and dLNs from WT recipients at 18 hours post-pHBV1.3/OVA323-339 HDI, showing S129G1_{HL} B cells (HuCk, blue) and endogenous B cells (IgD, brown). Scale bars, 50 μ m. **h-k** Representative histograms and geoMFI data of Nur77 expression in transferred S129G1_{HL} B cells in the spleens, dLNs, and livers from C3 KO (**h**, $n = 3$), Fc γ RIIB KO (**i**, $n = 3$), Zbtb46-DTR chimeras treated with DT (**j**, $n = 3$), and WT mice treated with CLD liposomes (**k**, $n = 3$), compared to their respective controls, at 21 hours post-pHBV1.3 HDI. At least two independent experiments were performed. The horizontal lines represent median values. Statistical significance was calculated using two-tailed Student's t -tests. Significance levels are indicated as **** $p < 0.0001$. Source data and exact p -values are available in the Source Data file.

these regions on day 2.5 (Fig. 6a, b). We observed a similar migratory pathway when we used SMARTA TCR transgenic T cells, specific for LCMV glycoprotein (GP) 66-80 epitope and injected the pHBV1.3/GP66-80 replicon (Supplementary Fig. 15d, e). By contrast, consistent with our previous report⁵², in the SRBC-OVA immunization model, splenic cDCs marked by DCIR2 re-localized from marginal zone bridging channels to the outer T cell zone, and nearly the entire population of activated OT-II T cells co-localized with the activated DCIR2⁺ cDCs (Supplementary Fig. 15f, g). Together, these findings reveal that B cells present antigens to CD4⁺ T cells through a series of interactions first in the follicles and then in the interfollicular regions of the spleen and dLNs, suggesting an alternative to the traditional view that CD4⁺ T cells are primed in T cell zones by cDCs^{13,21}.

CCR5 and EBI2 guide the follicular and interfollicular priming of CD4⁺ T cells by B cells, respectively

To identify the cues that might guide B cell and T cell migration and mediate their interactions, we conducted RNA-seq analysis on the

transferred S129G1_{HL} B cells in the spleen 18 hours after pHBV1.3/OVA323-339 injection. This revealed that the genes encoding CCL3 and CCL4 were most significantly induced (Fig. 7a and Supplementary Data 4), both of which are ligands for the chemokine receptor CCR5 on naive CD4⁺ T cells⁵⁵. These were the only upregulated chemokine genes in S129G1_{HL} B cells (Fig. 7b). Treatment of the mice with maraviroc, a commonly used CCR5 antagonist^{56,57}, halted OT-II T cell migration towards S129G1_{HL} B cells in follicles and hindered their activation after injection of pHBV1.3/OVA323-339 (Fig. 7c–e). Our previous work identified a key role for the oxysterol receptor EBI2 and its ligand, 7 α ,25-dihydroxycholesterol, in positioning activated T cells and cDC2 cells in the outer T cell zone⁵². Similarly, both EBI2 KO S129G1_{HL} B cells and EBI2 KO OT-II T cells failed to concentrate in interfollicular regions, instead localizing to the central T-B border (Fig. 7f, g) or the T cell zone (Fig. 7h, i), respectively. EBI2-deficient OT-II T cells proliferated less rapidly than WT OT-II T cells (Fig. 7j), which might be due to impaired interactions with their cognate WT B cells in the interfollicular regions. In summary, these findings establish that B cells present the antigen to

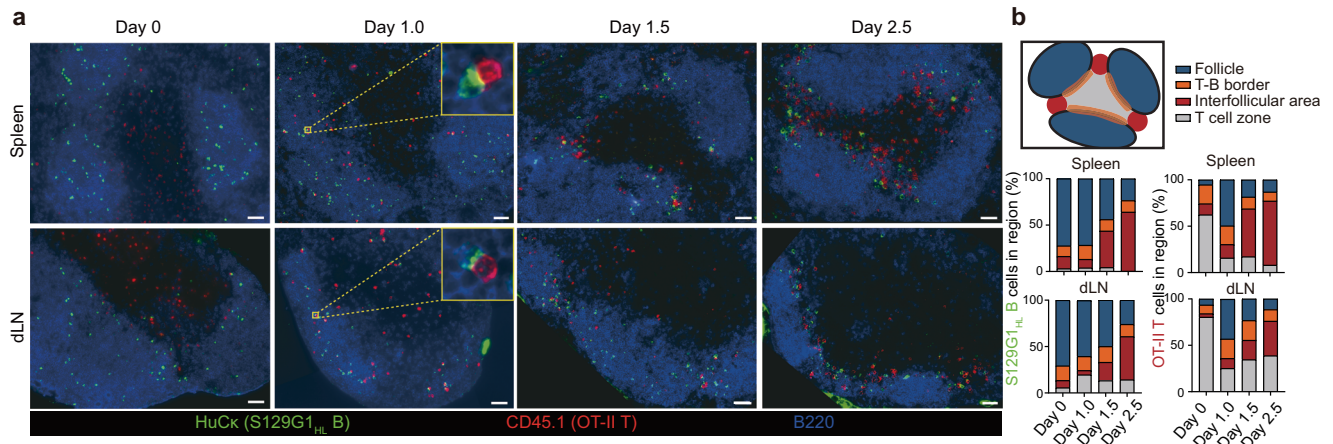


Fig. 6 | B cells initiate CD4⁺ T cell responses sequentially in follicular and interfollicular areas. **a** Immunofluorescence of S129G1_{HL} B cells (HuCk, green), OT-II T cells (CD45.1, red), and endogenous B cells (B220, blue) in the spleens and dLNs of WT recipients at the indicated time points post-pHBV1.3/OVA323-339 HDI. The boxed area indicates regions shown at higher magnification. Scale bars, 50 μ m. **b** Schematic illustration of the spatial organization of B and T cell zones and their

interfaces in spleen and dLN (top), and the relative proportions of S129G1_{HL} B cells (bottom, left) and OT-II T cells (bottom, right) localized in each anatomical region at the indicated time points. (middle: $n = 6$ white pulp areas from 3 mice; bottom: $n = 6$ LN slices from 6 mice). The data represent the relative proportions of each group. Three independent experiments were performed. Source data are available in the Source Data file.

CD4⁺ T cells first in follicular areas guided by the chemokine receptor CCR5, likely binding its ligands CCL3 and CCL4, and subsequently in interfollicular areas, guided by the oxysterol receptor EBI2 and its ligand 7 α ,25-dihydroxycholesterol.

Deciphering the cellular crosstalk landscape associated with T cell priming

The above results demonstrated that cDC1s and B cells drove CD8⁺ T and CD4⁺ T cell responses against HBsAg, respectively. We next set out to identify the signals provided by antigen-presenting cells to initiate T cell responses in addition to recognition of MHC-peptide complex by TCR. To do so, we used the NicheNet algorithm to prioritize ligand-receptor interactions between interacting antigen-presenting cells-T cells based on their bulk or single-cell transcriptome data. We first compared the single-cell transcriptome of CD11c^{high}MHCII⁺ DCs, hepatocytes and OT-I T cells in liver between day 0 and day 2.5 after the hydrodynamic injection of pHBV1.3/OVA257-264 (Supplementary Fig. 3a). Then, we built up a cDC1-proliferating CD8⁺ T cell ligand-receptor interaction map with NicheNet algorithm (Fig. 8a). We blocked those potential integrins and co-stimulatory pathways including CD86-CD28 and ALCAM-CD6 in *in vitro* co-culture system of cDC1s and CD8⁺ T cells (Fig. 8b). Intriguingly, CD8⁺ T cell proliferation induced by mature cDC1s was not affected by the CTLA4-Ig fusion protein (Fig. 8c), suggesting a weaker role for CD28 co-stimulation in priming CD8⁺ T cells than CD4⁺ T cells as has been previously reported^{58,59}. Consistent with previous observations that CD6 was a T cell co-stimulatory receptor^{60,61}, the presence of the recombinant soluble CD6-Fc molecules greatly inhibited CD8⁺ T cell proliferation (Fig. 8c). Notably, ALCAM mRNA was highly enriched in cDC1s, and moderately expressed in cDC2s and virus-infected hepatocytes, but not in other DC subsets, Kupffer cells and LSECs (Fig. 8a). Moreover, cDC1s constitutively expressed ALCAM protein at homeostasis (Supplementary Fig. 16a), with expression levels unaffected by pHBV1.3 hydrodynamic injection (Supplementary Fig. 16b). While LSECs also constitutively expressed ALCAM (Supplementary Fig. 16c), they co-expressed the immuno-inhibitory checkpoint PD-L1 (Supplementary Fig. 16d), consistent with previous reports^{62,63}, and their ALCAM expression decreased after pHBV1.3 hydrodynamic injection (Supplementary Fig. 16e). However, hepatocytes did not express ALCAM under either condition (Supplementary Fig. 16f, g). These findings may partially explain why only cDC1s were capable of priming CD8⁺ T cell responses. Additionally, scRNA-seq data from liver

biopsy of a patient with acute HBV infection revealed the presence of ALCAM mRNA in cDC1s (Supplementary Fig. 16h), suggesting a potential role for ALCAM in co-stimulating CD8⁺ T cell responses by human hepatic cDC1s. Together, these results demonstrated a CD6-dependent but CD28-independent co-stimulation mechanism for CD8⁺ T cell priming uniquely mediated by cDC1s.

Next, we sorted the S129G1_{HL} B and OT-II T cells interacting at follicular and interfollicular regions of spleens, corresponding to days 1 and 2.5 time points (Fig. 6a), respectively, and performed RNA-seq analysis (Supplementary Fig. 17a). According to the expression of ligands, receptors, associated pathway components and genomic targets of these pathways, we identified the top predicted the ligand-receptor pairs between B cells and CD4⁺ T cells (Fig. 9a and Supplementary Fig. 17b). Nearly half of these ligand-receptor pairs were shared by cells interacting at follicular and interfollicular regions (Supplementary Fig. 17c). Furthermore, we focused on blocking those shared integrin and co-stimulatory signals individually by using commercially available neutralizing antibodies or proteins in mice, considering their well-appreciated roles in T cell priming⁶⁴. The proliferation and survival of CD4⁺ T cells were strongly inhibited by an anti-LFA-1 (encoded by *Itgb2*) blocking antibody (Fig. 9b, c). The differentiated CD4⁺ T cells showed a compensatory increase in frequency but still decreased in total number (Fig. 9d). The competitive blockade of CD28-CD80 costimulatory pathway by a CTLA4-Ig fusion protein potently suppressed CD4⁺ T cell proliferation (Fig. 9e) and subsequently decreased the total number of differentiated T cells without any significant effect on survival and differentiation itself (Fig. 9f, g). However, the CD4⁺ T cell priming remained intact in mice treated with a widely used anti-ICOS antibody to block ICOSL engagement of ICOS (Supplementary Fig. 17d-f), which was believed to be an important co-stimulatory molecule for optimal CD4⁺ T cell responses⁶⁵. Additionally, we sorted HBsAg-specific B cells from PBMCs of four patients and performed scRNA-seq analysis, revealing increased expression of *Itgb2* (encoding LFA-1) and CD80 mRNA in activated B cells, along with upregulation of HLA-II genes (Supplementary Fig. 17g), suggesting a potential role for these molecules in co-stimulating CD4⁺ T cell responses by B cells in humans. These results indicated an LFA-1- and CD80-dependent but ICOSL-independent priming of CD4⁺ T cells by B cells. In sum, we mapped the ligand-receptor signaling landscape between antigen-presenting cells and T cells, identifying fundamental co-stimulatory signals required for optimal T cell responses to HBsAg.

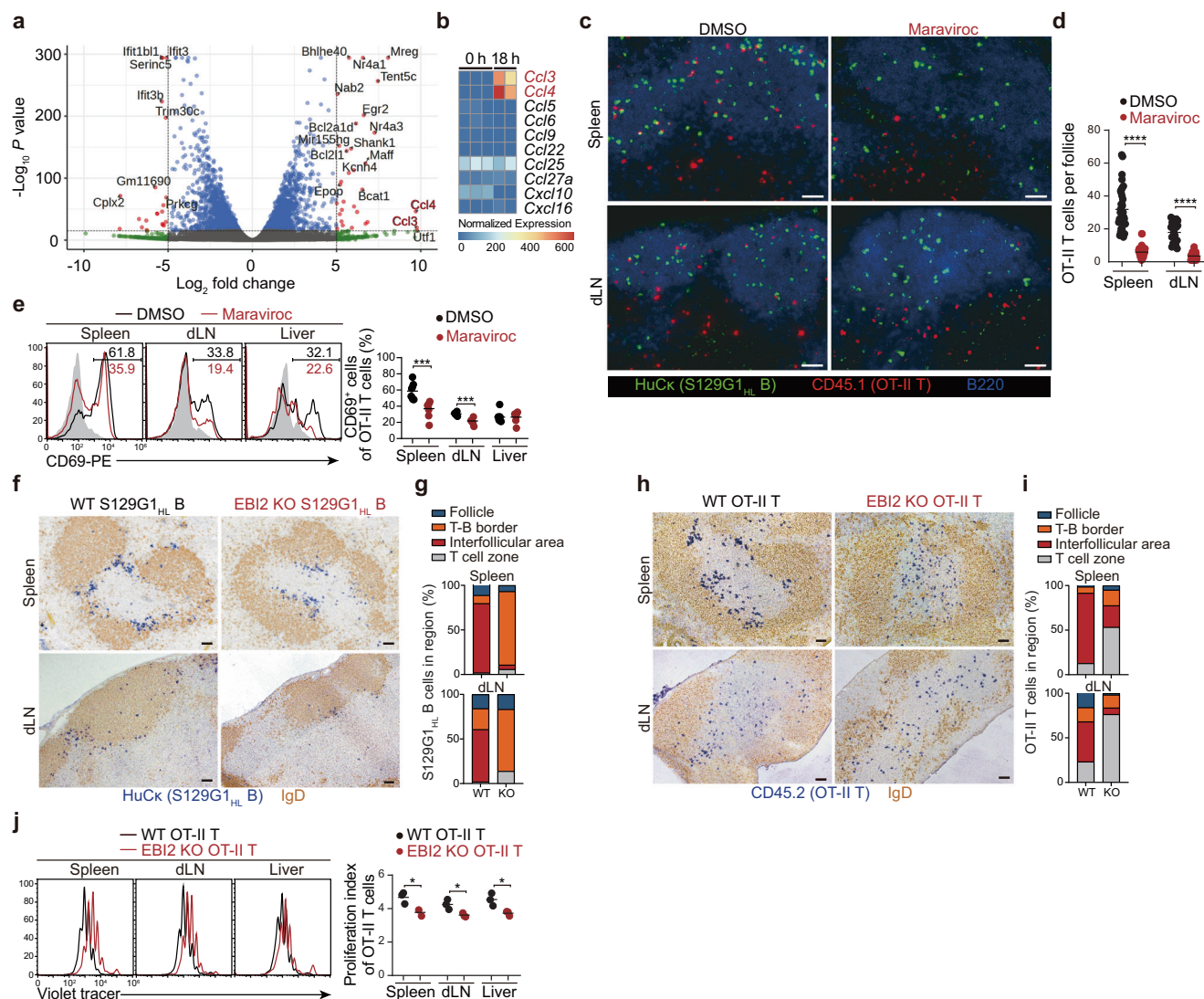


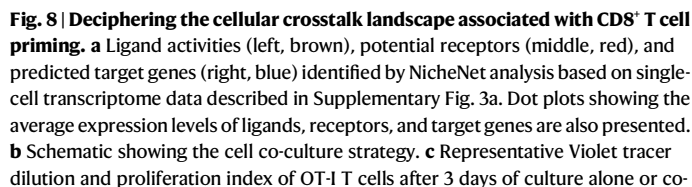
Fig. 7 | CCR5 and EBI2 guide the follicular and interfollicular priming of CD4⁺ T cells by B cells, respectively. **a** Volcano plot of RNA-seq showing differentially expressed genes in sorted S129G1_{HL} B cells at 18 versus 0 hours post-pHBV1.3 HDI. **b** RNA-seq heat map of chemokine gene expression in S129G1_{HL} B cells at 0 and 18 hours post-pHBV1.3 HDI. **c** Immunofluorescence of S129G1_{HL} B cells (HuCk, green), OT-II T cells (CD45.1, red), and endogenous B cells (B220, blue) in the spleens and dLNs of WT recipients treated with Maraviroc versus DMSO at day 1 post-pHBV1.3/OVA323-339 HDI. **d** Percentages of OT-II T cells within B cell follicles in (c) ($n = 40$ follicles from 3 mice). **e** Representative histograms and percentages of CD69⁺ OT-II T cells in spleens, dLNs, and livers from (c) ($n = 7$). **f** Immunohistochemistry of spleens and dLNs from WT recipients at day 2.5 post-pHBV1.3/OVA323-339 HDI, showing WT or EBI2 KO S129G1_{HL} B cells (HuCk, blue) and endogenous B cells (IgD, brown). **g** Quantification of WT and EBI2 KO S129G1_{HL} B cells in (f) (top: $n = 6$ white pulp areas from 3 mice; bottom: $n = 6$ LN slices from 6 mice). **h** Immunohistochemistry of spleens and dLNs from WT recipients at day 2.5 post-pHBV1.3/OVA323-339 HDI, showing WT or EBI2 KO OT-II T cells (CD45.2, blue) and endogenous B cells (IgD, brown). **i** Quantification of WT and EBI2 KO OT-II T cells in (h) (top: $n = 6$ white pulp areas from 3 mice; bottom: $n = 6$ LN slices from 6 mice). **j** Representative FACS plots and proliferation index of EBI2 KO versus WT OT-II T cells in spleens, dLNs, and livers from WT recipients at day 3.5 post-pHBV1.3/OVA323-339 HDI ($n = 3$). At least two independent experiments were performed. Horizontal lines of (d, e–j) represent median values. Data in g, i represent the relative proportions of each group. Statistical significance for data in g, e, j was calculated using two-tailed Student's *t*-tests. Significance levels are indicated as: * $p < 0.05$, *** $p < 0.001$, **** $p < 0.0001$. Scale bars (c, f, h), 50 μm . Source data and exact *p*-values are available in the Source Data file.

Together, these findings elucidate how HBsAg initiates T cell responses in HBV infection, revealing novel intercellular antigen presentation mechanisms distinct from classical viral paradigms (Supplementary Fig. 18).

Discussion

Understanding the ‘who,’ ‘where,’ and ‘how’ of antigen presentation to T cells is fundamental to deciphering the mechanisms that drive T cell immune responses. This study reveals novel intercellular mechanisms of HBsAg presentation that differ from those of viruses with broad tropisms, and those of model antigens. First, we show that the Batf3⁺XCR1⁺CCR7⁺ cDC1s drive the CD8⁺ T cell response against HBsAg

in the liver by acquiring HBsAg peptide-MHC-I complexes from irradiation-resistant cells, particularly LSECs, and presenting them to CD8⁺ T cells by the non-canonical antigen presentation mechanism known as MHC-I cross-dressing⁵⁰. Second, we show that, beyond their conventional antibody-secretion function, B cells are the principal antigen-presenting cells that prime CD4⁺ T cell responses against HBsAg by presenting antigens on MHC-II. These findings challenge the conventional paradigm that cDCs, especially cDC2s, initiate CD4⁺ T cell responses^{13,21}. Third, we show that B cells acquire nonopsonized HBsAg directly in situ in B cell follicles of the spleen and dLNs; the B cells then present the antigen to CD4⁺ T cells first in follicular areas guided by the chemokine receptor CCR5, and subsequently in interfollicular areas,



culture with liver-sorted cDC1s from WT mice hydrodynamically injected with pHBV1.3/OVA257-264 for 24 hours, in the presence of indicated proteins ($n = 3$ biologically independent replicates). Three independent experiments were performed. Statistical significance was calculated using one-way ANOVA with Tukey's multiple comparisons test for **c**. Error bars represent mean \pm SD, with significance levels indicated as: * $p < 0.05$. Source data and exact p -values are available in the Source Data file.

The liver provides niches for CD8⁺ T cell response, but the underlying mechanism remains largely unknown^{38–40,42,67}. In HBV transgenic mice, a non-inflamed model of chronic HBV infection, hepatocytes directly present antigens to virus-specific naive CD8⁺ T cells, initially triggering vigorous in situ proliferation but ultimately failing to induce IFN- γ production or cytolytic effector function due to the lack of necessary co-stimulatory signals^{38,42}. In our study, we provide strong evidence that intrahepatic resident Batf3⁺XCRI⁺CCR7⁺cDC1s drive the CD8⁺ T cell proliferation and differentiation via MHC-I cross-dressing in pHBV1.3, prcccDNA, AdHBV, AAV8-HBV mouse models, which exhibit different degrees of inflammation, from strong to mild. Thus, these findings raise the possibility that cDC1 cross-dressing may not occur in the absence of inflammation but is instead triggered under specific inflammatory conditions. However, the specific inflammatory molecules involved, and the exact mechanism remain to be elucidated. An intriguing avenue for further study would be to investigate how MHC-I-peptide complexes are transferred from LSECs or hepatocytes to cDC1s, using imaging and genetic approaches in an inflammatory context. Additionally, it would be insightful to examine whether and how HBV manipulates the antigen presentation pathway of cDC1 cross-dressing to establish chronic infection.

hepatocytes, express ALCAM at both mRNA and protein levels at homeostasis. While LSECs also express ALCAM, they co-express the inhibitory checkpoint PD-L1. By utilizing cross-dressing as a novel mode of antigen presentation to T cells in the liver, cDC1s bypass the co-stimulation defects of hepatocytes and the co-inhibitory activity of LSECs, which can lead to T cell anergy or impaired proliferation and differentiation^{40,42}. This also eliminates the need for direct antigen uptake and processing. Additionally, while DC cross-dressing has been shown to be important for anti-tumor, anti-viral, and anti-allograft immunity in certain contexts^{68–71}, studies on cross-dressing in hepatic diseases remain limited. Notably, graft-infiltrating PD-L1^{hi} cross-dressed DC may play a key role in the induction of liver transplant tolerance⁷². However, the role of cDC1 cross-dressing in liver inflammation, fibrosis, cancer, and other hepatic diseases remains largely unexplored. This gap in knowledge highlights the need for targeted research to elucidate the impact of cDC1 cross-dressing across these conditions.

12

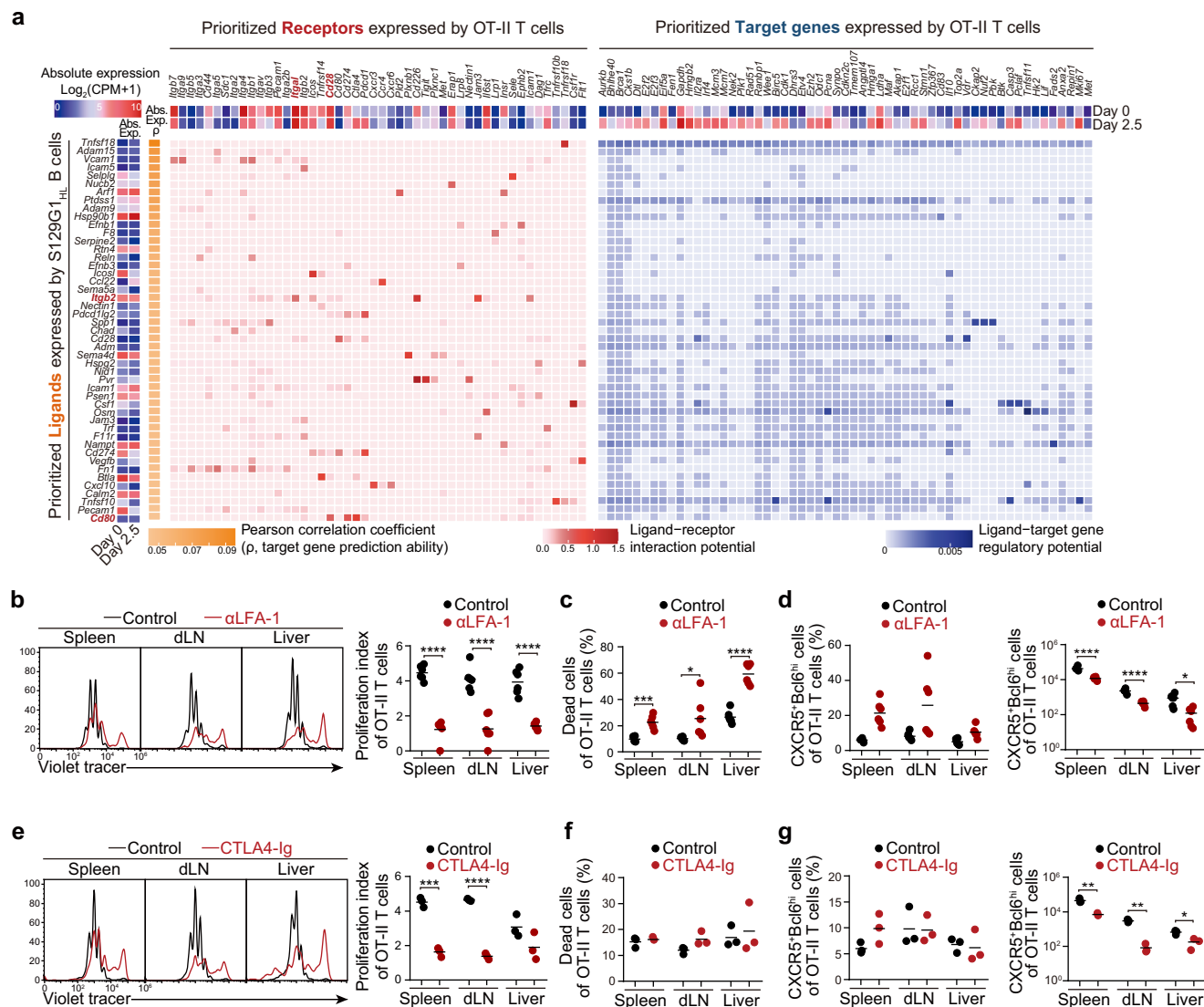


Fig. 9 | Deciphering the cellular crosstalk landscape associated with CD4⁺ T cell priming. **a** Ligand activities (left, brown), potential receptors (middle, red), and predicted target genes (right, blue) identified by NicheNet analysis based on the key signature genes of transferred OT-II T cells in spleens from WT mice, at day 2.5 post-HDI of pHBV1.3/OVA323-339. Heatmaps showing the absolute expression levels of ligands, receptors, and target genes are also shown. **b** Representative Violet tracer dilution and proliferation index of OT-II T cells at day 3.5 in the spleens, dLNs, and livers from WT mice treated with anti-Itgb2/LFA1 antibody versus control antibodies, at day 3.5 post-HDI of pHBV1.3/OVA323-339 ($n = 6$). **c** Percentages of dead cells within transferred OT-II T cells in spleens, dLNs, and livers from the mice

described in **(b)** using the viability dye eFluor 780 ($n = 6$). **d** Percentages and number of CXCR5^{hi}Bcl6^{hi} cells within transferred OT-II T cells in spleens, dLNs, and livers from the mice described in **(b)**, ($n = 6$). **e** Same as **(b)**, but mice were treated with control or CTLA4-Ig protein ($n = 3$). **f** Same as **c**, but mice were treated with control or CTLA4-Ig protein ($n = 3$). **g** Same as **(d)**, but mice were treated with control or CTLA4-Ig protein ($n = 3$). At least two independent experiments were performed. Horizontal lines indicate median values. Statistical significance was calculated using two-tailed Student's *t*-tests. Significance levels are indicated as: * $p < 0.05$, ** $p < 0.01$, *** $p < 0.001$, **** $p < 0.0001$. Source data and exact *p*-values are available in the Source Data file.

specific CD8⁺ T cells via cross-presentation, thereby enhancing their antiviral function upon interleukin-2 administration³⁹. This highlights the need to investigate whether the priming of HBcAg- and polymerase-specific CD8⁺ T cells in the liver involves cDC1 cross-dressing during acute HBV infection. If not, identifying the antigen-presenting cells responsible for their priming and elucidating the underlying mechanisms remains a critical direction for future research.

The paradigm that cDCs dominate CD4⁺ T cell responses was recently challenged by studies showing that B cells are the predominant antigen-presenting cells that initiate naive CD4⁺ T cell responses during *Plasmodium* infection and when RNA phage Qβ-derived virus-like particles were used as a model antigen^{73,74}. In this study, we provide strong evidence that B cells, not cDCs, are the

antigen-presenting cells that initiate the CD4⁺ T cell responses against HBsAg. Whereas cDCs take up antigens mostly by binding to non-specific receptors, B cells uptake antigens that bind to antigen-specific BCRs, potentially making B cells more efficient antigen-presenting cells than cDCs at the individual cell level. Importantly, viruses can cross-link the BCR of antigen-specific B cells through multivalent interactions with the particulate and highly repetitive protein antigens of viruses, thereby strongly inducing expression of co-stimulatory molecules²⁰. If viruses or certain particulate antigens enter cDCs efficiently by natural infection, as do live influenza viruses or by endocytosis, as in sheep red blood cells^{52,75}, cDCs might act as the primary antigen-presenting cells for CD4⁺ T cell responses against them. HBV does not infect cDCs, however, and HBsAg is reported to inhibit activation of cDCs⁷⁶, suggesting that cDCs probably do not capture HBsAg

and present it to CD4⁺ T cells efficiently. Therefore, cDCs and B cells might both prime CD4⁺ T cells depending on their relative abilities to present antigen and to activate the cells. Notably, studies have reported that HBsAg-specific B cells exhibit an anergic state in patients with chronic HBV^{77,78}, indicating that these B cells may lose their ability to initiate CD4⁺ T cell responses during the persistence of HBsAg.

Many studies of model antigen transport and presentation to B cells have found that they are transported passively through the blood or lymph to the spleen and LNs, where they pass through a filter that excludes antigen complexes larger than approximately 5.5 nm¹⁴. These large antigen complexes, including opsonized antigens cannot diffuse passively into lymphoid follicles but must be actively transported by accessory or resident cells¹⁷. We were surprised to find that HBsAg, which circulates in 22 nm subviral particles, bypasses opsonization and the size filter of the conduit system to gain access direct to the follicles in the early stage of infection. One possible explanation could be that circulating HBsAg is degraded to a size small enough to bypass the filter mechanism, thereby gaining access to follicular B cells without the involvement of CD169⁺ macrophages or DCs. However, considering that T cell assistance for B cells to respond to HBsAg operates through an intermolecular mechanism⁷⁹, we consider this explanation to be highly unlikely. Alternatively, the virus infection might result in extracellular matrix remodeling and/or conduit system disruption to permit the entry of large particles⁸⁰.

In this study, we utilized several mouse models to explore the mechanisms of HBsAg presentation relevant to T cell responses. Although these models do not perfectly replicate the dynamics of human HBV infection, they provide valuable insights into specific aspects of viral immunopathogenesis^{25,31,32,81}. Notably, we observed similarities in liver cell clusters between humans and mice, as previously reported⁴⁵, suggesting that shared features may exist in the immune responses to HBV in both systems. In line with this, cDC1s, which are associated with CD8⁺ T cell responses against HBV in the human liver, were shown to drive CD8⁺ T cell proliferation and differentiation in the mouse liver. Consistent with the critical role of ALCAM-CD6 co-stimulation in mouse cDC1-mediated CD8⁺ T cell responses, hepatic cDC1s also expressed ALCAM mRNA in at least one human liver sample. Furthermore, aligning with the observation that cDC2s may be ineffective in initiating CD4⁺ T cell responses in acute HBV patients, our data revealed that B cells, rather than cDCs, initiate CD4⁺ T cell responses against HBsAg. In mice, CD4⁺ T cell priming relied on co-stimulatory signals, including *Itgb2* (encoding LFA-1) and *CD80*. These molecules were similarly upregulated in HBsAg-specific B cells from the PBMCs of four acute HBV patients. However, the extent to which these mouse models fully capture the complexity of HBV-related immunology in humans remains unclear. Nevertheless, our findings challenge traditional concepts of viral antigen presentation and lay the groundwork for innovative therapeutic strategies to combat chronic HBV infection.

Methods

Mice and bone marrow chimaeras

The HBsAg-specific Ig knock-in S129G1_{HL} mice were generated on a C57BL/6 background by CRISPR-Cas9-mediated targeting of a bicistronic allele encoding both the light and the heavy Ig chains to the endogenous Igh locus as previously described⁸², with the assistance of Cyagen Biosciences. The light and heavy Ig chains were derived from the 129G1 monoclonal antibody recognizing a linear epitope located at amino acids 137–151 of HBsAg⁵³, with a HuCk used for subsequent identification of cells bearing the transgenic receptor. The S129G1_{HL} allele can be identified by PCR using the primer sets: S129G1_{HL} Forward: 5'-CTGATAGGCACCAAGTACACTA-3', S129G1_{HL} Reverse: 5'-GCTATAGCAACCACTTGTAGGTG-3'. The *Ebi2*^{-/-} mice were generated by CRISPR-Cas9-mediated homologous recombination in mouse ES cells on an albino C57BL/6 background with assistance from Cyagen Biosciences.

The *Ebi2* Mutant allele can be distinguished from the WT allele by PCR using the primer sets: *Ebi2* Common Forward: 5'-CAGCTGGTGTAGGTACACACCTAC-3', *Ebi2* Wildtype Reverse: 5'-CTCCGTAATGACACACAATCATC-3' and *Ebi2* Mutant Reverse: 5'-TTCAGTGTGCAAATTCCTCG-3'. WT C57BL/6 mice (Stock no. N000013) and BALB/c mice (Stock no. N000020) were purchased from GemPharmatech. CD45.1⁺ congenic C57BL/6 mice (stock No. 002014), *Irfa*^{fl/fl} mice (stock No. 009380), B cell-deficient μ MT mice (stock No. 002288), *MHC-II*^{-/-} mice (stock No. 003584), HBV Env28 TCR transgenic mice (stock No. 027510), Zbtb46-DTR (stock No. 019506) for the specific depletion of cDCs, cDC1-deficient *Batf3*^{-/-} mice (stock No. 013755), monocyte-deficient *Ccr2*^{-/-} mice (stock No. 004999), OVA-specific TCR transgenic OT-II mice (stock No. 004194) and OT-I mice (stock No. 003831), HEL-specific BCR transgenic MD4 mice (stock No. 002595), LCMV GP61-80 TCR-specific transgenic SMARTA mice (stock No. 030450), LCMV GP33-41 TCR-specific transgenic P14 mice (stock No. 037394), *C3*^{-/-} mice (stock No. 029661), and *Itgax*^{Cre} mice (stock No. 008068) were purchased from the Jackson Laboratory. VSV-specific BCR transgenic VII0YEN mice were provided by M. Iannacone⁸³. HEL-specific BCR knock-in Hy10 mice were provided by J. Cyster⁸⁴. *H2-Ab1*^{fl/m1} LysMCre mice, with *Mhc-II* conditional knockout in phagocytes, were provided by T. Deng⁸⁵. *Rab27a*^{fl/m} Rosa26CreERT2 mice, with the tamoxifen-induced knockout of *Rab27a*, were provided by Z. Cai⁸⁵. *FcyRIIIB*^{-/-} mice were provided by F. Li⁸⁶. β 2M^{-/-} mice, characterized by severely diminished MHC-I expression, were provided by S. Yu⁸⁷. F1 (C57BL/6 X BALB/c) mice were provided by C. Duan. *Irfa*^{fl/fl} mice were crossed to *Itgax*^{Cre} mice to obtain cDC2-deficient *Irfa*^{fl/fl}CD11cCre mice. Bone marrow chimeras were generated as previously described⁵² and subsequently analyzed after a period of 6–12 weeks. All mice were maintained at a 12-h light-dark cycle, at a temperature of 64–72 °F (18–22 °C), and at a humidity condition of 30–70% at the Laboratory Animal Research Center of Shanghai Medical College, Fudan University. All mice were euthanized following the CO₂ euthanasia protocol. All experiments were conducted using six- to eight-week-old male mice, with experimental groups matched for age and housing conditions. Each group of mice was co-housed separately. All the animal studies were approved by the Ethics Committee of the School of Basic Medical Sciences, Fudan University (Approval No: 20190221-098) and the Ethics Committee of Pudong Hospital, Shanghai (Approval No: 2021-DS-M-20).

Human specimens

Human tissue samples were obtained from Huashan Hospital of Fudan University in compliance with national guidelines. All patients met the diagnostic criteria for acute HBV infection and had no prior history of HBV infection. Specifically, HBsAg positivity was detected within 2 to 14 days after the onset of symptoms, during which there were no anti-HBs antibodies present, but positive anti-HBc antibodies were observed. Follow-up assessments lasting up to four months indicated that all patients achieved clearance of HBV DNA and HBsAg, while developing HBsAg-specific antibodies and maintaining anti-HBc antibodies. Comprehensive clinical characteristics of the patients are presented in Supplementary Data 1. The study was approved by the Institutional Review Board at Huashan Hospital (Ethics Committee Archiving No. KY2021-919). All patients provided written informed consent. Human PBMCs from healthy donors and patients with acute HBV infection were isolated and cryopreserved. The isolation of immune cells from liver puncture biopsy was performed as previously described⁸⁸.

HBV surrogate mouse models

The original pHBV1.3 HBV replicon construct was previously described⁴⁸. We created a recombinant pHBV1.3 HBV replicon expressing HBsAg fused to OVA323-339 epitope (pHBV1.3/OVA323-339), by silencing all original HBsAg⁸⁹, followed by the insertion of an HBsAg-reading frame with an embedded OVA323-339 fragment between 127 and 128 amino acids of S gene. The pHBV1.3/GP66-80 and

pHBV1.3/OVA257-264 were constructed by replacing OVA323-339 with GP66-80 and OVA257-264, respectively. The secretion-deficient HBsAg (Cys48Ala) was previously described⁸⁹. The pHBV1.3/OVA257-264-IRES-ZsGreen was constructed by inserting IRES-ZsGreen sequence amplified from pHAGE-CMV-hIL7-IRES-ZsGreen (Addgene, 26532) to the pHBV1.3/OVA257-264. The pALB-Igk/HEL construct was engineered to express HEL under the hepatocyte-specific ALB promoter, incorporating an Igk leader sequence at the N-terminus to facilitate secretion. The pALB-Igk/HEL-OVA257-264 construct was created by insertion of OVA257-264 fragment at the C-terminus of the HEL gene. For hydrodynamic injection, a total of 20 µg plasmid was diluted in 2 ml of saline and injected into the tail vein of 6- to 8-week-old mice within 5–8 seconds, as described previously⁴⁸. For low-dose administration, 0.5 µg of plasmid was diluted in the same volume of saline. The prcccDNA plasmid was described previously³¹. To establish acute infection, we hydrodynamically co-injected 4 µg of pCMV-Cre and 8 µg of prcccDNA, resulting in recombinant cccDNA generation in mouse hepatocytes. The AdHBV were produced, propagated, and titrated as described earlier³². High-dose and low-dose infections were induced by intravenous (i.v.) injection of 3×10^9 i.u. and 1×10^8 i.u. of AdHBV in 200 µL of saline, respectively³². For the AAV-HBV mouse model, each mouse was i.v. injected with 5×10^{10} AAV-HBV.

LCMV infection and SRBC-OVA immunization

The LCMV Armstrong strain, provided by M. Matloubian, was propagated using standard procedures. Mice were administered 2×10^5 plaque-forming units (PFU) of LCMV Armstrong via intraperitoneal injection. Simultaneously, OVA-conjugated SRBCs were prepared and injected intraperitoneally (i.p.) at a dose of 2×10^8 SRBCs, following previously established methods⁵².

Sucrose-gradient ultracentrifugation and electron microscopy

Human hepatoma cell lines Huh7 were cultured and transfected with pHBV1.3/OVA323-339 plasmid. Continuous sucrose density gradients (10, 20, 30, 40, 50 and 60%) were prepared with a solution containing 20 mM Tris-HCl (pH 7.4), 140 mM NaCl, and 1 mM EDTA. Culture supernatant was concentrated by PEG 8000, followed by laid on the linear sucrose gradient and centrifugation at $200,000 \times g$ for 14 hours at 4 °C with a Beckman SW 41 Ti rotor. Fractions were collected from top to bottom, and the density of each fraction was determined by refractometry (Abbe 60). Fractions containing HBsAg were determined with an HBsAg ELISA kit (Shanghai Kehua Bio-Engineering Co.). For electron microscopy of HBsAg particles, purified particles were fixed with 2% glutaraldehyde and dropped onto a carbon-coated copper grid. Grids were contrasted with phosphoric tungstic acid and examined by a CM120 transmission electron microscope (Phillips)⁹⁰.

Serum HBsAg and HBsAg-specific IgG detection

Sera were prepared from blood collected from the retro-orbital sinus of the mouse at the indicated time points. Serum levels of HBsAg were quantified using chemiluminescence immunoassay (CLIA) kits (Auto-bio), following the manufacturer's guidelines. Serum levels of anti-HBsAg antibodies were monitored by indirect ELISA after 1:100 dilution with PBS containing 2% BSA. Plates were coated with the recombinant ayw-specific and CHO cell-derived HBsAg proteins (Bioforce) at 100 ng per well, and nonspecific binding was blocked with PBS containing 2% BSA. Then, 100 µl of diluted serum samples were added to the reaction well and incubated for 60 minutes at 37 °C, followed by washing and reaction with horseradish peroxidase (HRP)-conjugated anti-mouse IgG antibody (Jackson ImmunoResearch Labs). After the addition of chromogenic substrate solution for 30 minutes, the reaction was terminated by the addition of an acidic stop solution. The absorbance of each well was read at 450 nm by a microplate reader (Bio-Rad X-Mark spectrophotometer).

Cell isolation, labeling, and adoptive transfer

T cells from OT-II, SMARTA, OT-I, P14, and Env28 mice, along with B cells from S129G_{HL}, Hy10, and VII0YEN mice, were isolated from the spleens and LNs using commercial isolation kits (BioLegend, STEM-CELL). Cell proliferation was visualized by labeling the isolated cells with CellTrace™ Violet Tracer (Thermo Fisher Scientific) as per the manufacturer's instructions. For the analysis of T and B cell activation and proliferation, 6×10^6 isolated cells or 1×10^6 labeled cells were adoptively transferred. For the analysis of T cell differentiation, 1×10^6 T cells were transferred for early time points (day 3 or day 3.5), while 2×10^5 T cells were transferred for a later time point (day 7). To observe CD4⁺ T and B cell interactions, either 1.2×10^7 B cells or 6×10^6 T cells were transferred for visualization at 18 hours, day 1 and day 1.5 post-injection, or 7.2×10^6 B cells and 3.6×10^6 T cells were transferred for visualization at day 2.5 post-injection. In the MHC-II dependency experiment, 1×10^7 B cells from either WT or MHC-II KO mice were transferred to µMT recipients. In the MHC-I dependency experiment, 5×10^5 FACS-sorted cDC1s from WT or β2M KO donors were transferred to Batf3 KO recipients.

In vivo treatments

Heterozygous Zbtb46-DTR full chimeras underwent cDC ablation through intraperitoneal (i.p.) injection of 20 ng/g body weight diphtheria toxin (DT; Sigma-Aldrich) 3 days prior to hydrodynamic injection or infection, and continued on a regimen of 4 ng/g body weight DT every 3 days. Total macrophage depletion involved intravenous administration of CLD liposomes (FormuMax) according to the manufacturer's instructions. Exosome depletion was facilitated by treating Rab27a^{fl/fl} Rosa26CreERT2 mice with tamoxifen (2.5 mg/mouse/day, Sigma-Aldrich) for 3 days, starting 7 days before hydrodynamic injection. Blocking antibodies such as anti-XCL1 (50 µg/mouse, 80222, R&D Systems), anti-CLEC9A (100 µg/mouse, 7H11, BioXCell), anti-ICOS (200 µg/mouse, clone 7E.17G9, BioXCell) and anti-LFA-1 (200 µg/mouse, M17/4, BioXCell) were administered i.v. every 3 days, starting 2 days prior to hydrodynamic injection or infection. To prevent B-cell re-entry into the splenic white pulp, mice were injected i.v. with anti-VLA-4 (200 µg/mouse, clone PS/2, BioXCell) and anti-LFA-1 at 200 µg per mouse 2 hours as described⁵⁴ after hydrodynamic injection of pHBV1.3. To prevent OT-I T cell entry into LNs, anti-CD62L antibody (200 µg/mouse, Mel-14, BioXCell) was administered i.v. every 3 days, beginning 4 hours before the transfer. Antibodies used are detailed in Supplementary Table 1. To prevent T and B cell egress from LNs, FTY720 was injected i.p. at a dose of 1 µg/g body weight, 4 hours after T cell or B cell transfer. The initial interaction between T and B cells was blocked by daily i.p. administration of the CCR5 antagonist maraviroc (200 µg/g body weight, Selleck), starting 4 hours before the transfer. Splenectomy was conducted at 2 hours after pHBV1.3 hydrodynamic injection, with a control group undergoing sham operation involving spleen exteriorization and manipulation for at least 30 seconds. To competitively block the CD28-CD80 costimulatory pathway, the mouse was injected i.v. with recombinant CTLA4-Ig (clone CTLA4-Ig, ZXBio) fusion proteins at 200 µg/mouse one day prior to cell transfer and thereafter every 3 days. For the administration of EdU, mice were treated with EdU (Beyotime) in PBS via i.p. injection at a dosage of 50 mg/kg body weight, administered daily for 5 consecutive days prior to euthanasia. The 129G1 monoclonal antibody (1 mg/mouse) was administered i.v. to mice that had received a hydrodynamic injection of pHBV1.3 two days earlier. All commercial reagents used are detailed in Supplementary Table 2.

Flow cytometry and cell sorting

Single-cell suspensions were prepared from mouse spleens, dLNs, or livers as previously described^{38,91}. Fc receptors were blocked using 2.5 µg/mL purified anti-CD16/32 (BioLegend) at 4 °C for 15 minutes. Live/dead cell discrimination was performed using Live/Dead Fixable

Viability Dye eFluor 780 (eBioscience). Surface antibodies used in this study were as follows: CXCR5 (2G8), B220 (RA3-6B2), CD103 (2E7), CD11b (M1/70), CD11c (N418), CD138 (281-2), ALCAM (eBioALC48), PD-L1 (10 F.9G2), OX40 (OX-86), CD19 (6D5), CD3 (17A2), CD31 (MEC13.3), CD4 (GK1.5), CD45.1 (A20), CD64 (X54-5/7.1), CD8 α (53-6.7), F4/80 (BM8), H-2K^b bound to SIINFEKL (25-D1.16), human Ig light chain κ (MHK-49), I-Ab (AF6-120.1), Ly6C (HK1.4), TCR V α 2 (B20.1), XCR1 (ZET), CD25 (PC61.5), CD45.2 (104), CD69 (HL2F3), H-2K^b (AF6-88.5.5.3), H-2K^d (SF1-1.1.1). CXCR5 and H-2K^b-ENV353 (VWLSVIWM) tetramer primary staining occurred at room temperature for 30–45 minutes, with all other surface staining at 4 °C for 30 minutes. Fluorescently labeled streptavidin was used to detect biotinylated antibodies. For the Antigen-Specific Immune Response (AIM) assay, single-cell suspensions were rested at 37 °C for 3 hours before seeding at 1×10^6 cells/well in U-bottom 96-well plates. Cells were then stimulated with 5 μ g/ml of each 18mer peptide of a peptide pool spanning HBsAg for 18 hours at 37 °C. For intracellular staining, T cells were stimulated with HBsAg peptide pool for 18 hours, or cell stimulation cocktail (eBioscience) for 4 hours at 37 °C. The cells were then harvested, stained for surface markers, and subsequently fixed and permeabilized using the Intracellular Fixation & Permeabilization Buffer Set (eBioscience). Intracellular staining for IFN- γ (XMGL2) and GzmB (NGZB) was performed at 4 °C for 30 minutes. For intranuclear staining, cells already stained for surface markers were fixed and permeabilized using the Foxp3/Transcription Factor Staining Buffer Set (eBioscience). Intranuclear staining of Bcl6 (IG191E/A8), T-bet (4B10), and Nur77 (12.14) was subsequently performed at 4 °C overnight. HBsAg-binding B cells were detected using HBsAg (Bioforce) labeled by Alexa Fluor 647 (Invitrogen). HEL-binding B cells were detected using HEL (Sigma-Aldrich) labeled by Alexa Fluor 647. All antibodies for flow cytometry were purchased from BioLegend, Thermo Fisher Scientific, or BD Biosciences, with flow cytometry performed using the BD LSRFortessa or Attune NxT (Thermo Fisher Scientific). The incorporation of EdU into cellular nucleic acids was detected using the BeyoClick EdU Cell Proliferation Kit with Alexa Fluor 647 (Beyotime) according to the manufacturer's instructions. For cell sorting, cells were stained using the same method as in the flow cytometry protocol, with CD45.1-enrichment applied when necessary. The sorted cells included various types such as CD11c^{high}MHC-II⁺ pan-DCs, CD11c^{high}MHC-II⁺XCR1⁺ cDC1s, CD11c^{high}MHC-II⁺CD11b⁺ cDC2s, CD11c^{high}MHC-II⁺F4/80⁺ mono-DCs, CD11c^{low}MHC-II⁺ F4/80⁺ Kupffer cells and CD31⁺ LSECs, B220⁺CD45.1⁺HuC κ ⁺ S129G1_{HL} B cells, CD45.1⁺CD4⁺TCR V α 2⁺ OT-II cells and CD45.1⁺CD8⁺TCR V α 2⁺ OT-I cells. All these cells were sorted on a BD FACSAria IIu. The flow cytometric gating strategies are indicated in the Supplementary Fig. 19. Data were analyzed with FlowJo software (Tree Star, Inc. version 10.8.1). Antibodies used are detailed in Supplementary Table 1.

Ex vivo co-culture assay

To obtain specific DC subsets or other APC compartments, cells were FACS-sorted from livers of mice as described above. To obtain CD8⁺ T cells, TCR transgenic CD8⁺ T cells were isolated from spleens and LNs of naïve OT-I mice and stained with CellTrace™ violet tracer as described above. For the co-culture, 1×10^5 CellTrace™ violet-labeled TCR transgenic T cells and 5×10^4 sorted antigen-presenting cells were individually mixed and added to each well of a U-bottom tissue culture-treated 96-well plate in RPMI1640 supplemented with 10% FBS, 1% penicillin/streptomycin, and $1 \times$ HEPES. For competitive blocking of ALCAM-CD6 and CD80-CD28 pathways, 10 μ g/ml mouse recombinant CTLA4-Ig fusion protein (clone CTLA4-Ig, ZXBio) and mouse recombinant CD6 protein (Sino Biological Inc.) were added to the culture medium, respectively. Cells were cultured at 37 °C and 5% CO₂ for 3 days. T cell proliferation was then measured by dye dilution via flow cytometry. For the in vitro assay to assess SIINFEKL-MHC-I complexes transfer from LSECs and hepatocytes, these cells were isolated from

the livers of naïve mice and stimulated overnight with IFN- γ (200 ng/ml, PeproTech). Subsequently, they were loaded with 1 μ g/ml OVA257-264 (SIINFEKL) peptide for 1 hour at 37 °C. After thorough washing, the cells were co-cultured with FACS-sorted cDC1s at 37 °C for 18 hours, and the proportion of H-2K^b-SIINFEKL⁺ cDC1s was quantified using flow cytometry.

Immunohistochemistry and immunofluorescent microscopy

For immunohistochemistry, tissues were directly frozen in OCT. Cryosections of 7 μ m were dried for 20 minutes at room temperature, fixed in 4 °C acetone for 10 minutes, dried for 1 hour at room temperature and stained immunohistochemically as previously described⁵² with Rabbit anti-HBsAg (Bio-Rad), FITC-conjugated anti-IgD (11-26 c.2a), biotin-conjugated anti-HuC κ (MHK-49) or biotin-conjugated anti-CD45.2 (104) antibody for 2–3 hours at room temperature, followed by HRP-conjugated anti-rabbit IgG, HRP-conjugated anti-FITC or AP-conjugated Streptavidin (Jackson ImmunoResearch) for 1–2 hours at room temperature. Liver sections were counterstained in Hematoxylin. Images were captured with a BX63 Upright Microscope (Olympus). For immunofluorescent microscopy, tissues expressing ZsGreen were fixed in 4% PFA for 2 hours at 4 °C, washed, and sunk in 30% sucrose before being frozen in OCT. All other tissues were directly frozen in OCT, and slides were fixed in ice acetone. For hematoxylin and eosin (H&E) staining, the liver sections were stained from formalin-fixed, paraffin-embedded tissues. Cryosections of 7 μ m were stained as previously described⁵² with Super Bright 436-conjugated anti-B220 (RA3-6B2), biotin-conjugated anti-human Ig light chain κ (1:50 dilution, MHK-49), biotin-conjugated anti-DCIR2 (33D1), biotin-conjugated 35.61 antibody (European Virus Archive Global), Alexa Fluor 647-conjugated anti-CD45.1 (A20) antibodies overnight at 4 °C, followed by Alexa Fluor 488-conjugated anti-FITC, Alexa Fluor 488-conjugated anti-Rabbit IgG, Cy3-conjugated anti-biotin, Cy3-conjugated anti-Rat IgG (Jackson ImmunoResearch), Alexa Fluor 647-conjugated anti-Rabbit IgG (Invitrogen) and APC Streptavidin (BioLegend) for 1–2 hours at room temperature. Antibodies used are detailed in Supplementary Table 1. For staining of DCIR2, a tyramide amplification kit was used (TSA Biotin System; Perkin Elmer). Subsequently, DAPI (Sigma Aldrich) was applied for 15 minutes at room temperature. All commercial reagents used are detailed in Supplementary Table 2. Images were captured with a BX63 Upright Microscope (Olympus) equipped with a Prime BSI sCMOS Camera (Photometrics).

Bulk RNA-seq and data analysis

Sorted cells ($>10^5$) were snap frozen, and then RNA was extracted with the RNeasy Mini Kit (QIAGEN). RNA was checked by gel electrophoresis and quantified with a Qubit Fluorometer (Invitrogen). Barcoded sequencing libraries were constructed using the TruSeq Stranded mRNA kit (Illumina). Sequencing was performed on an Illumina NovaSeq 6000 System (Geneng Biotechnology) with 150 bp paired-end reads. The raw data was handled by Skewer (v0.2.2), and data quality was checked by FastQC (v0.11.5). Clean reads were aligned to the mm10 mouse genome with STAR (v2.7.9a) and counted with featureCounts (v2.0.1). Generation of differentially expressed genes was defined based on a logFC cutoff >1 or <-1 and adj.P value < 0.05 with DESeq2 (v1.30.1) using R software (v4.0.3).

scRNA-seq and data analysis

For human specimens, frozen samples were thawed, recovered, and washed using RPMI1640 medium supplemented with 10% FBS, and then labeled by TotalSeq anti-human Hashtag (BioLegend). Single cells were captured using the 10 x Chromium (10x Genomics), and libraries were prepared using Chromium Next GEM Single Cell 5' Reagent Kits v2 (10x Genomics), according to the manufacturer's instructions. Libraries were run on an Illumina NovaSeq 6000 System (Geneng

Biotechnology) for 150 bp paired-end sequencing. Raw gene expression matrices were generated by the Cell Ranger (v5.0) pipeline coupled with human reference version GRCh38. The output filtered gene expression matrices were analyzed by R software (v4.0.3) with the Seurat package (v4.0.2). Low-quality cells with less than 200 detected genes, as well as cells with more than 10% mitochondrial gene counts and 5% hemoglobin gene counts, or potential doublets with UMI counts above 10,000 were filtered out. Hashtag-labeled cells were demultiplexed with HTODemux function to identify their original samples. UMI counts were then normalized with the SCTransform function.

To integrate cells into a shared space from different datasets for unsupervised clustering, we used the Seurat's SelectIntegrationFeatures function to identify 3000 features with high cell-to-cell variation, then identified "anchors" between individual datasets with the FindIntegrationAnchors function and inputted these anchors into the IntegrateData function to do batch effect correction. Then, the integrated dataset was scaled, and PCA was calculated. The first 50 PCs were used to construct an SNN network, and a graph-based clustering approach, Louvain algorithm, was applied to identify cell clusters with the resolution = 1. Finally, uniform manifold approximation and projection (UMAP) was applied to visualization. The first round of clustering identified 6 major cell types, including CD4⁺ T cells, CD8⁺ T cells, NK cells, B cells, hepatocytes, and myeloid cells. To identify clusters within each major cell type, we performed a second round of clustering on CD4⁺ T cells, CD8⁺ T cells, B cells, and myeloid cells separately. Marker genes were identified with Seurat's FindAllMarkers function. Clusters were then classified and annotated based on expressions of canonical markers of particular cell types. Clusters expressing two or more canonical cell-type markers were classified as doublet cells and excluded from further analysis.

Generation of DEGs was defined based on the adj.P value < 0.05 with Seurat's FindMarkers function using "MAST" test. GSEA of the DEGs was conducted with the clusterProfiler's (v3.18.1) gseGO, gseKEGG, gsePathway, gseWP, and GSEA function. Gene sets were limited by minSize = 3 and maxSize = 500. GO over-representation analysis of the DEGs was conducted with the enrichGO function. Log2 transformed relative T cell proportion changes were calculated by dividing the fraction of the cell type in an individual patient by the mean of healthy donors. Signature module scores were calculated with Seurat's AddModuleScore function using default settings. We used 9 cytotoxicity-associated genes (PRF1, IFNG, GNLY, NKG7, GZMB, GZMA, GZMK, GZMH, and FASLG) to define the inflammation scores. PROGENy model (v1.17.3) and DoRothEA (v1.8.0) were used to infer pathway and TF activity between AHB and HD groups of T cells via decoupleR (v2.2.2). The activity scores were inferred by running Weighted Mean (WMEAN) with the run_wmean function. Single-cell TCRs were computed from the sequencing data using Cell Ranger.

For samples from mice, immediately post-sorting, cells from different organs or time points were labeled by TotalSeq anti-mouse Hashtag (BioLegend) separately. Single cells were captured using the 10x Chromium (10x Genomics), and libraries were prepared using Chromium Next GEM Single Cell 3' Reagent Kits v3.1 (10x Genomics) according to the manufacturer's instructions. Raw gene expression matrices were generated by the Cell Ranger pipeline, as described above, coupled with the mouse reference version mm10. The output filtered gene expression matrices were analyzed by R software with the Seurat package. Low-quality cells or potential doublets were filtered out. Hashtag-labeled cells were demultiplexed with the HTODemux function to identify their original organs or time points. UMI counts were then normalized with the SCTransform function. PCA was calculated and used to construct an SNN network. A graph-based clustering approach was applied to identify cell clusters with a resolution = 0.6. Clusters were then classified and annotated based on expressions of canonical markers of particular cell types.

Image quantification

For quantifying IHC images, HBsAg-positive hepatocytes were automatically counted using the Positive cell detection function in QuPath (v.0.3.2) as previously described⁹². This was done across a total of 15 view fields, with five randomly selected fields per mouse at 20× magnification. The intensity threshold parameters were manually adjusted for each experimental group, ensuring identical procedures for all samples. Antigen-specific B and T cell positioning within lymphoid tissue regions was quantified as detailed⁹³. SI29G1_{HL} B and OT-II T cell counts in these regions were manually executed with CellSens (v.2.3). Stacked bar charts were subsequently calculated and designed with GraphPad Software (v. 8.4.3).

Statistical analysis

Statistical analysis was performed with GraphPad Software (v. 8.4.3) and R softwares (v4.0.3). Unpaired two-tailed Student's *t*-test was used for comparisons between two groups. Two-way ANOVA test with Šidák multiple testing correction was used for serum HBV antigen assays. Fisher's exact test was used for odds ratio of expanded T cells between AHBs and HDs. Differences between groups were considered significant for *p* values < 0.05 (* *p* < 0.05; ** *p* < 0.01; *** *p* < 0.001; **** *p* < 0.0001). No statistical methods were used to predetermine sample size, which was chosen based on prior experience with a similar experimental design.

Reporting summary

Further information on research design is available in the Nature Portfolio Reporting Summary linked to this article.

Data availability

Mouse bulk-RNA-seq data generated during this study have been deposited in the Gene Expression Omnibus (GEO) at the National Center for Biotechnology Information (NCBI) under the accession code [GSE207539](#). Mouse scRNA-seq data have been deposited in GEO under the accession code [GSE207541](#). Human scRNA-seq data have been deposited in the Open Archive for Miscellaneous Data (OMIX) at the China National Center for Bioinformatics under the accession code [OMIX009529](#). Source data are provided with this paper.

References

- Hsu Y. C., Huang D. Q. & Nguyen M. H. Global burden of hepatitis B virus: current status, missed opportunities and a call for action. *Nat. Rev. Gastroenterol. Hepatol.* **20**, 524–537 (2023).
- Seeger, C. & Mason, W. S. Hepatitis B virus biology. *Microbiol. Mol. Biol. Rev.* **64**, 51–68 (2000).
- Nassal, M. HBV cccDNA: viral persistence reservoir and key obstacle for a cure of chronic hepatitis B. *Gut* **64**, 1972–1984 (2015).
- Dienstag, J. L. Hepatitis B virus infection. *N. Engl. J. Med.* **359**, 1486–1500 (2008).
- Iannaccone M. & Guidotti L. G. Immunobiology and pathogenesis of hepatitis B virus infection. *Nat. Rev. Immunol.* **22**, 19–32 (2021).
- Guidotti, L. G., Isogawa, M. & Chisari, F. V. Host-virus interactions in hepatitis B virus infection. *Curr. Opin. Immunol.* **36**, 61–66 (2015).
- Wieland, S., Thimme, R., Purcell, R. H. & Chisari, F. V. Genomic analysis of the host response to hepatitis B virus infection. *Proc. Natl. Acad. Sci. USA* **101**, 6669–6674 (2004).
- Stacey, A. R. et al. Induction of a striking systemic cytokine cascade prior to peak viremia in acute human immunodeficiency virus type 1 infection, in contrast to more modest and delayed responses in acute hepatitis B and C virus infections. *J. Virol.* **83**, 3719–3733 (2009).
- Rehermann, B., Ferrari, C., Pasquinelli, C. & Chisari, F. V. The hepatitis B virus persists for decades after patients' recovery from acute viral hepatitis despite active maintenance of a cytotoxic T-lymphocyte response. *Nat. Med.* **2**, 1104–1108 (1996).

10. Lim, S. G. et al. The scientific basis of combination therapy for chronic hepatitis B functional cure. *Nat. Rev. Gastroenterol. Hepatol.* **20**, 238–253 (2023).
11. Moini, M. & Fung, S. HBsAg loss as a treatment endpoint for chronic HBV infection: HBV cure. *Viruses* **14**, 657 (2022).
12. Qi, H., Kastenmuller, W. & Germain, R. N. Spatiotemporal basis of innate and adaptive immunity in secondary lymphoid tissue. *Annu Rev. Cell Dev. Biol.* **30**, 141–167 (2014).
13. Durai, V. & Murphy, K. M. Functions of murine dendritic cells. *Immunity* **45**, 719–736 (2016).
14. Cyster, J. G. B cell follicles and antigen encounters of the third kind. *Nat. Immunol.* **11**, 989–996 (2010).
15. Guillems, M. et al. Dendritic cells, monocytes and macrophages: a unified nomenclature based on ontogeny. *Nat. Rev. Immunol.* **14**, 571–578 (2014).
16. Worbs, T., Hammerschmidt, S. I. & Forster, R. Dendritic cell migration in health and disease. *Nat. Rev. Immunol.* **17**, 30–48 (2017).
17. Heesters, B. A., van der Poel, C. E., Das, A. & Carroll, M. C. Antigen presentation to B cells. *Trends Immunol.* **37**, 844–854 (2016).
18. Zhou, X., Ramachandran, S., Mann, M. & Popkin, D. L. Role of lymphocytic choriomeningitis virus (LCMV) in understanding viral immunology: past, present and future. *Viruses* **4**, 2650–2669 (2012).
19. Abdel-Hakeem, M. S. Viruses teaching immunology: Role of LCMV model and human viral infections in immunological discoveries. *Viruses* **11**, 106 (2019).
20. Zabel, F., Kundig, T. M. & Bachmann, M. F. Virus-induced humoral immunity: on how B cell responses are initiated. *Curr. Opin. Virol.* **3**, 357–362 (2013).
21. Crotty, S. T follicular helper cell differentiation, function, and roles in disease. *Immunity* **41**, 529–542 (2014).
22. McCall, L. I., Siqueira-Neto, J. L. & McKerrow, J. H. Location, location: five facts about tissue tropism and pathogenesis. *PLoS Pathog.* **12**, e1005519 (2016).
23. Schneider-Schaulies, J. Cellular receptors for viruses: links to tropism and pathogenesis. *J. Gen. Virol.* **81**, 1413–1429 (2000).
24. Tzeng, H. T., Hsu, P. N. & Chen, P. J. Immunocompetent non-transgenic mouse models for studying hepatitis B virus immune responses. *J. Gastroenterol. Hepatol.* **28**, 116–119 (2013).
25. Hu, J., Lin, Y. Y., Chen, P. J., Watashi, K. & Wakita, T. Cell and Animal Models for Studying Hepatitis B Virus Infection and Drug Development. *Gastroenterology* **156**, 338–354 (2019).
26. Bosch, M. et al. A liver immune rheostat regulates CD8 T cell immunity in chronic HBV infection. *Nature* **631**, 867–875 (2024).
27. Shen, Z. et al. Hepatitis B virus persistence in mice reveals IL-21 and IL-33 as regulators of viral clearance. *Nat. Commun.* **8**, 2119 (2017).
28. Guidotti, L. G. et al. Immunosurveillance of the liver by intravascular effector CD8(+) T cells. *Cell* **161**, 486–500 (2015).
29. Wang, X. et al. Dysregulated response of follicular helper T cells to Hepatitis B surface antigen promotes HBV persistence in mice and associates with outcomes of patients. *Gastroenterology* **154**, 2222–2236 (2018).
30. Li, G. et al. Recombinant covalently closed circular DNA of hepatitis B virus induces long-term viral persistence with chronic hepatitis in a mouse model. *Hepatology* **67**, 56–70 (2018).
31. Qi, Z. et al. Recombinant covalently closed circular hepatitis B virus DNA induces prolonged viral persistence in immunocompetent mice. *J. Virol.* **88**, 8045–8056 (2014).
32. Huang, L. R. et al. Transfer of HBV genomes using low doses of adenovirus vectors leads to persistent infection in immune competent mice. *Gastroenterology* **142**, 1447–1450.e1443 (2012).
33. Yang, D. et al. A mouse model for HBV immunotolerance and immunotherapy. *Cell Mol. Immunol.* **11**, 71–78 (2014).
34. Salomon, B. L. Insights into the biology and therapeutic implications of TNF and regulatory T cells. *Nat. Rev. Rheumatol.* **17**, 487–504 (2021).
35. White, L. C. et al. Regulation of LMP2 and TAP1 genes by IRF-1 explains the paucity of CD8+ T cells in IRF-1^{-/-} mice. *Immunity* **5**, 365–376 (1996).
36. Davey, M. S. et al. The human Vdelta2(+) T-cell compartment comprises distinct innate-like Vgamma9(+) and adaptive Vgamma9(-) subsets. *Nat. Commun.* **9**, 1760 (2018).
37. Becher, B., Tugues, S. & Greter, M. GM-CSF: From growth factor to central mediator of tissue inflammation. *Immunity* **45**, 963–973 (2016).
38. Benechet, A. P. et al. Dynamics and genomic landscape of CD8(+) T cells undergoing hepatic priming. *Nature* **574**, 200–205 (2019).
39. De Simone, G. et al. Identification of a Kupffer cell subset capable of reverting the T cell dysfunction induced by hepatocellular priming. *Immunity* **54**, 2089–2100.e2088 (2021).
40. Murata, Y., Kawashima, K., Sheikh, K., Tanaka, Y. & Isogawa, M. Intrahepatic cross-presentation and hepatocellular antigen presentation play distinct roles in the induction of Hepatitis B virus-specific CD8(+) T cell responses. *J. Virol.* **92**, e00920-18 (2018).
41. Cho, Y. B., Lee, I. G., Joo, Y. H., Hong, S. H. & Seo, Y. J. TCR transgenic mice: a valuable tool for studying viral immunopathogenesis mechanisms. *Int J. Mol. Sci.* **21**, 9690 (2020).
42. Isogawa, M., Chung, J., Murata, Y., Kakimi, K. & Chisari, F. V. CD40 activation rescues antiviral CD8(+) T cells from PD-1-mediated exhaustion. *PLoS Pathog.* **9**, e1003490 (2013).
43. Isogawa, M., Furuichi, Y. & Chisari, F. V. Oscillating CD8(+) T cell effector functions after antigen recognition in the liver. *Immunity* **23**, 53–63 (2005).
44. Ebrahimkhani, M. R., Mohar, I. & Crispe, I. N. Cross-presentation of antigen by diverse subsets of murine liver cells. *Hepatology* **54**, 1379–1387 (2011).
45. Donovan, M. K. R., D’Antonio-Chronowska, A., D’Antonio, M. & Frazer, K. A. Cellular deconvolution of GTEx tissues powers discovery of disease and cell-type associated regulatory variants. *Nat. Commun.* **11**, 955 (2020).
46. Colbert, J. D., Cruz, F. M. & Rock, K. L. Cross-presentation of exogenous antigens on MHC I molecules. *Curr. Opin. Immunol.* **64**, 1–8 (2020).
47. Ostrowski, M. et al. Rab27a and Rab27b control different steps of the exosome secretion pathway. *Nat. Cell Biol.* **12**, 19–30 (2010).
48. Li, J. et al. Exosomes mediate the cell-to-cell transmission of IFN- α -induced antiviral activity. *Nat. Immunol.* **14**, 793–803 (2013).
49. Sancho, D. et al. Identification of a dendritic cell receptor that couples sensing of necrosis to immunity. *Nature* **458**, 899–903 (2009).
50. Campana, S., De Pasquale, C., Carrega, P., Ferlazzo, G. & Bonaccorsi, I. Cross-dressing: an alternative mechanism for antigen presentation. *Immunol. Lett.* **168**, 349–354 (2015).
51. Carestia, A. et al. Modulation of the liver immune microenvironment by the adeno-associated virus serotype 8 gene therapy vector. *Mol. Ther. Methods Clin. Dev.* **20**, 95–108 (2021).
52. Li, J., Lu, E., Yi, T. & Cyster, J. G. EBI2 augments Tfh cell fate by promoting interaction with IL-2-quenching dendritic cells. *Nature* **533**, 110–114 (2016).
53. Zhang, T. Y. et al. Prolonged suppression of HBV in mice by a novel antibody that targets a unique epitope on hepatitis B surface antigen. *Gut* **65**, 658–671 (2016).
54. Lo, C. G., Lu, T. T. & Cyster, J. G. Integrin-dependence of Lymphocyte Entry into the Splenic White Pulp. *J. Exp. Med.* **197**, 353–361 (2003).
55. Griffith, J. W., Sokol, C. L. & Luster, A. D. Chemokines and chemokine receptors: positioning cells for host defense and immunity. *Annu Rev. Immunol.* **32**, 659–702 (2014).
56. Joy, M. T. et al. CCR5 Is a Therapeutic Target for Recovery after Stroke and Traumatic Brain Injury. *Cell* **176**, 1143–1157.e1113 (2019).
57. Martin-Blondel, G., Brassat, D., Bauer, J., Lassmann, H. & Liblau, R. S. CCR5 blockade for neuroinflammatory diseases—beyond control of HIV. *Nat. Rev. Neurol.* **12**, 95–105 (2016).

58. Andreassen, S. O., Christensen, J. E., Marker, O. & Thomsen, A. R. Role of CD40 ligand and CD28 in induction and maintenance of antiviral CD8⁺ effector T cell responses. *J. Immunol.* **164**, 3689–3697 (2000).
59. Grujic, M. et al. The role of CD80/CD86 in generation and maintenance of functional virus-specific CD8⁺ T cells in mice infected with lymphocytic choriomeningitis virus. *J. Immunol.* **185**, 1730–1743 (2010).
60. Gimferrer, I. et al. Relevance of CD6-mediated interactions in T cell activation and proliferation. *J. Immunol.* **173**, 2262–2270 (2004).
61. Zimmerman, A. W. et al. Long-term engagement of CD6 and ALCAM is essential for T-cell proliferation induced by dendritic cells. *Blood* **107**, 3212–3220 (2006).
62. Diehl, L. et al. Tolerogenic maturation of liver sinusoidal endothelial cells promotes B7-homolog 1-dependent CD8⁺ T cell tolerance. *Hepatology* **47**, 296–305 (2008).
63. Crispe, I. N. Liver antigen-presenting cells. *J. Hepatol.* **54**, 357–365 (2011).
64. Attanasio, J. & Wherry, E. J. Costimulatory and coinhibitory receptor pathways in infectious disease. *Immunity* **44**, 1052–1068 (2016).
65. Choi, Y. S. et al. ICOS receptor instructs T follicular helper cell versus effector cell differentiation via induction of the transcriptional repressor Bcl6. *Immunity* **34**, 932–946 (2011).
66. Yadav, T., Kumar, S., Mishra, G. & Saxena, S. K. Tracking the COVID-19 vaccines: The global landscape. *Hum. Vaccin Immunother.* **19**, 2191577 (2023).
67. Bohm, W. et al. Exogenous hepatitis B surface antigen particles processed by dendritic cells or macrophages prime murine MHC class I-restricted cytotoxic T lymphocytes in vivo. *J. Immunol.* **155**, 3313–3321 (1995).
68. Martinez-Usatorre, A. & De Palma, M. Dendritic cell cross-dressing and tumor immunity. *EMBO Mol. Med.* **14**, e16523 (2022).
69. Hughes, A. D. et al. Cross-dressed dendritic cells sustain effector T cell responses in islet and kidney allografts. *J. Clin. Invest* **130**, 287–294 (2020).
70. Duong, E. et al. Type I interferon activates MHC class I-dressed CD11b(+) conventional dendritic cells to promote protective anti-tumor CD8(+) T cell immunity. *Immunity* **55**, 308–323.e309 (2021).
71. MacNabb, B. W. et al. Dendritic cells can prime anti-tumor CD8(+) T cell responses through major histocompatibility complex cross-dressing. *Immunity* **55**, 2206–2208 (2022).
72. Ono, Y. et al. Graft-infiltrating PD-L1(hi) cross-dressed dendritic cells regulate antidonor T cell responses in mouse liver transplant tolerance. *Hepatology* **67**, 1499–1515 (2018).
73. Arroyo E. N. & Pepper M. B cells are sufficient to prime the dominant CD4⁺ Tfh response to Plasmodium infection. *J. Exp. Med.* **217**, e20190849 (2020).
74. Hong, S. et al. B cells are the dominant antigen-presenting cells that activate naive CD4(+) T cells upon immunization with a virus-derived nanoparticle antigen. *Immunity* **49**, 695–708.e694 (2018).
75. Hong, S. et al. B cells are the dominant antigen-presenting cells that activate naive CD4⁺ T cells upon immunization with a virus-derived nanoparticle antigen. *Immunity* **49**, 695–708.e694 (2018).
76. Op den Brouw, M. L. et al. Hepatitis B virus surface antigen impairs myeloid dendritic cell function: a possible immune escape mechanism of hepatitis B virus. *Immunology* **126**, 280–289 (2009).
77. Burton, A. R. et al. Circulating and intrahepatic antiviral B cells are defective in hepatitis B. *J. Clin. Invest.* **128**, 4588–4603 (2018).
78. Salimzadeh, L. et al. PD-1 blockade partially recovers dysfunctional virus-specific B cells in chronic hepatitis B infection. *J. Clin. Invest.* **128**, 4573–4587 (2018).
79. Sette, A. et al. Selective CD4⁺ T cell help for antibody responses to a large viral pathogen: deterministic linkage of specificities. *Immunity* **28**, 847–858 (2008).
80. Gregory, J. L. et al. Infection programs sustained lymphoid stromal cell responses and shapes lymph node remodeling upon secondary challenge. *Cell Rep.* **18**, 406–418 (2017).
81. Yang, P. L., Althage, A., Chung, J. & Chisari, F. V. Hydrodynamic injection of viral DNA: a mouse model of acute hepatitis B virus infection. *Proc. Natl. Acad. Sci. USA* **99**, 13825–13830 (2002).
82. Jacobsen, J. T. et al. One-step generation of monoclonal B cell receptor mice capable of isotype switching and somatic hypermutation. *J. Exp. Med.* **215**, 2686–2695 (2018).
83. Hangartner, L. et al. Antiviral immune responses in gene-targeted mice expressing the immunoglobulin heavy chain of virus-neutralizing antibodies. *Proc. Natl. Acad. Sci. USA* **100**, 12883–12888 (2003).
84. Phan, T. G. et al. B cell receptor-independent stimuli trigger immunoglobulin (Ig) class switch recombination and production of IgG autoantibodies by anergic self-reactive B cells. *J. Exp. Med.* **197**, 845–860 (2003).
85. Blaszcak, A. M. et al. Loss of antigen presentation in adipose tissue macrophages or in adipocytes, but not both, improves glucose metabolism. *J. Immunol. (Baltim., Md: 1950)* **202**, 2451–2459 (2019).
86. Li, F. & Ravetch, J. V. Inhibitory Fcγ receptor engagement drives adjuvant and anti-tumor activities of agonistic CD40 antibodies. *Science* **333**, 1030–1034 (2011).
87. Steinke, F. C. et al. TCF-1 and LEF-1 act upstream of Th-POK to promote the CD4(+) T cell fate and interact with Runx3 to silence Cd4 in CD8(+) T cells. *Nat. Immunol.* **15**, 646–656 (2014).
88. Zheng, C. et al. Landscape of infiltrating t cells in liver cancer revealed by single-cell sequencing. *Cell* **169**, 1342–1356.e1316 (2017).
89. Li, J. et al. Subversion of cellular autophagy machinery by hepatitis B virus for viral envelopment. *J. Virol.* **85**, 6319–6333 (2011).
90. Bai, L. et al. Extracellular Hepatitis B Virus RNAs are heterogeneous in length and circulate as capsid-antibody complexes in addition to virions in chronic Hepatitis B patients. *J. Virol.* **92**, e00798-18 (2018).
91. Yi, T. et al. Oxysterol gradient generation by lymphoid stromal cells guides activated B cell movement during humoral responses. *Immunity* **37**, 535–548 (2012).
92. Bankhead, P. et al. QuPath: Open source software for digital pathology image analysis. *Sci. Rep.* **7**, 16878 (2017).
93. Kerfoot, S. M. et al. Germinal center B cell and T follicular helper cell development initiates in the interfollicular zone. *Immunity* **34**, 947–960 (2011).

Acknowledgements

We thank M. Iannaccone, H. Wang, K. Yang, F. Li and C. Huang for mice, S. Sun, Y. Wang and Y. Li for help with flow cytometry and cell sorting, and E. Dang, T. Yi and D. Liu for advice and review of the manuscript. This work was supported by the National Natural Science Foundation of China (82171747 to J. Li), the National Key R&D Program of China (2023YFC2306404 and 2024YFA1803102 to J. Li), the National Science and Technology Major Project of China (2018ZX10301202-002 to J. Li), the Shanghai Municipal Science and Technology Major Project (to J. Li), and the Non-profit Central Research Institute Fund of Chinese Academy of Medical Sciences (2023-PT310-02 to J. Li). Figures 1a, 3d, 3j, Supplementary Fig. S2a, S3a, S17a, and S18 were created with BioRender.com, under the agreement number QP281QMQUU.

Author contributions

X.L. and W. Sun designed and performed most of the experiments, interpreted the results, and prepared the manuscript. X.X. contributed to the HBV-replication assays. Q.J., W.Y., B.S. and J.Z. collected the clinical samples. Y.S., S.W. and H.Z. performed some of the flow cytometry experiments. J. Liu and W. Song helped with the reagents. Z.Y. provided some research resources. J. Li conceived of the study, designed experiments, supervised research and wrote the manuscript.

Competing interests

The authors declare no competing interests.

Additional information

Supplementary information The online version contains supplementary material available at <https://doi.org/10.1038/s41467-025-59985-8>.

Correspondence and requests for materials should be addressed to Zhenghong Yuan or Jianhua Li.

Peer review information *Nature Communications* thanks Gaetan Barbet, Robert Thimme, and the other anonymous reviewer(s) for their contribution to the peer review of this work. A peer review file is available.

Reprints and permissions information is available at <http://www.nature.com/reprints>

Publisher's note Springer Nature remains neutral with regard to jurisdictional claims in published maps and institutional affiliations.

Open Access This article is licensed under a Creative Commons Attribution-NonCommercial-NoDerivatives 4.0 International License, which permits any non-commercial use, sharing, distribution and reproduction in any medium or format, as long as you give appropriate credit to the original author(s) and the source, provide a link to the Creative Commons licence, and indicate if you modified the licensed material. You do not have permission under this licence to share adapted material derived from this article or parts of it. The images or other third party material in this article are included in the article's Creative Commons licence, unless indicated otherwise in a credit line to the material. If material is not included in the article's Creative Commons licence and your intended use is not permitted by statutory regulation or exceeds the permitted use, you will need to obtain permission directly from the copyright holder. To view a copy of this licence, visit <http://creativecommons.org/licenses/by-nc-nd/4.0/>.

© The Author(s) 2025